ABSTRACT

Title of dissertation: NANOPHOTONIC QUANTUM INTERFACE FOR A SINGLE SOLID-STATE SPIN

Shuo Sun, Doctor of Philosophy, 2016

Dissertation directed by: Professor Edo Waks
Department of Electrical and Computer Engineering

The ability to store and transmit quantum information plays a central role in virtually all quantum information processing applications. Single spins serve as pristine quantum memories whereas photons are ideal carriers of quantum information. Strong interactions between these two systems provide the necessary interface for developing future quantum networks and distributed quantum computers. They also enable a broad range of critical quantum information functionalities such as entanglement distribution, non-destructive quantum measurements and strong photon-photon interactions. Realizing spin-photon interactions in a solid-state device is particularly desirable because it opens up the possibility of chip-integrated quantum circuits that support gigahertz bandwidth operation.

In this thesis, I demonstrate a nanophotonic quantum interface between a single solid-state spin and a photon, and explore its applications in quantum information processing. First, we experimentally realize a spin-photon quantum phase switch based on a strongly coupled quantum dot and photonic crystal cavity sys-

tem. This device enables coherent light-matter interactions at the fundamental limit, where a single spin controls the polarization of a photon and a single photon flips the spin state. Furthermore, we theoretically propose a way to deterministically generate spin-photon entanglement based on the spin-photon quantum interface, which is an important step towards solid-state implementations of quantum repeaters and quantum networks. Next, we show both theoretically and experimentally, a new method to optically read out a solid-state spin based on the same cavity quantum electrodynamics (QED) system. This new method achieves significant improvement in spin readout fidelity over typical approaches using fluorescence light detection.

In the end, we report efforts to realize tunable and robust quantum dot based cavity QED systems. We present a technique for tuning the frequency of a quantum dot that is strongly coupled to a photonic crystal cavity by applying strain. This tuning technique enables us to accurately control the detuning between a quantum dot and a cavity without affecting other emission properties of the dot, which is essential for lots of applications associated with cavity QED systems, including non-classical light generation, photon blockade, single photon level optical switch, and also our major focus, the spin-photon quantum interface.

NANOPHOTONIC QUANTUM INTERFACE FOR A SINGLE SOLID-STATE SPIN

by

Shuo Sun

Dissertation submitted to the Faculty of the Graduate School of the
University of Maryland, College Park in partial fulfillment
of the requirements for the degree of
Doctor of Philosophy
2016

Advisory Committee:
Professor Edo Waks, Chair/Advisor
Professor Thomas E. Murphy
Professor Jeremy N. Munday
Professor Mohammad Hafezi
Professor Steven L. Rolston

Acknowledgments

Throughout the past five years, I am fortunate to work with many talented people who have helped and inspired me. First of all, I would like to thank my advisor, Professor Edo Waks, for his outstanding guidance and support. I enjoy every day that I have worked with him, from the beginning of my graduate study where he worked side by side with me on experimental instrumentations, towards the end where we spent hours discussing exciting new ideas. He has also taught me valuable lessons on effective writings and presentations, which I deeply value now. His great passion for research has led me a path towards an academic career in the future.

I would like to thank Professor Steven Rolston, Professor Thomas Murphy, Professor Jeremy Munday, and Professor Mohammad Hafezi for being on my dissertation defense committee. Special thanks go to Professor Thomas Murphy, who has offered great support and valuable advices in my applications for a future research position, and Professor Mohammad Hafezi, who has raised several insightful questions during my proposal exam and dissertation defense, which deepen my understandings on my own research. I would also like to thank Dr. Glenn Solomon, who is not only an important collaborator to our research, but also a great mentor to me.

I would like to acknowledge all of my friends and colleagues in the Waks group. In particular, I would like to thank Hyochul Kim for passing me with all of his hands-on experiences ranging from optical alignment to nano-fabrications. My first two

years working with him is a great pleasure and it is definitely a memorable time of mine. I also want to thank Tao Cai for generously letting me take as much lab time as I want during the time when I was desperate for obtaining the last piece of data for demonstrating the spin-photon quantum switch.

I acknowledge support from technicians in the UMD nanofabrication center: Tom Loughran, Jon Hummel, John Abrahams, Larry Lai and Wen-an Chiou. I thank them all for maintaining the equipments in a good shape and always being there to help when necessary. I would also like to thank all the staff members in IREAP and ECE, past and present, Jay Pyle, Nolan Ballew, Bryan Quinn, Joe Kselman, William Schuste, Ed Condon, Nancy Boone, Dorothea Brosius, Kathryn Tracey, Melanie Prange, Vivian Lu, Bill Churma, Emily Irwin, and Maria Hoo. Special thanks go to Jay Pyle who helped me design and make lots of useful mechanical components in my setup, and Nolan Ballew, Joe Kselman and Bryan Quinn who work closely with me regarding cooling waters and electricity supply.

I want to thank my family for their support and love throughout the years. Especially, I would like to thank my mom and dad who allow me the freedom to pursue what I enjoyed ever since I was a little boy. They were also great teachers when I was little, which are the initial reasons that drive me crazy about math and science. My final thanks goes to a girl whom I met in the fifth year of my graduate school. She is the most wonderful discovery in my life. Time with her is full of joy and surprise. I cannot wait to share the rest of my life with her.

Table of Contents

List of Figures

List of Abbreviations

QED	quantum electrodynamics
qubit	quantum bit
PBS	Polarization Beam Splitter
InAs	Indium Arsenide
GaAs	Gallium Arsenide
FDTD	finite-difference time-domain
SPCM	Single Photon Counting Module
LED	Light Emitting Diode

Chapter 1: Introduction

1.1 Overview

Interactions between spins and photons play a central role in the field of quantum information processing. Spin is a pristine quantum memory while photons are ideal carriers of quantum information. Efficient interfaces between these systems are essential for development of future quantum networks [1,2] and distributed quantum computers [3]. They also enable critical functionalities such as entanglement distribution [4, 5], non-destructive qubit measurements [6–8], and strong photon-photon interactions for photonic quantum computation [9, 10].

Solid-state nanophotonic devices provide a desirable platform for creating spin-photon interactions. These devices can be integrated on-a-chip to attain a compact architecture for quantum circuits [11, 12]. Many theoretical works have proposed exploiting the strong light-matter interactions inherent to nanophotonic waveguides and cavities to create a spin-photon interface [13–19]. In this approach, a single spin modulates the optical transmission or reflection of the nanophotonic structure, thereby switching an incident photon. However, such a spin-photon interface has yet to be realized.

The spin of a singly charged quantum dot has attracted significant interest

for implementing a solid-state spin-photon interface. This trapped spin system provides a promising quantum memory with microsecond coherence time [20, 21] and picosecond timescale single-qubit gates [21–26], enabling a large number of quantum operations prior to qubit decoherence. Furthermore, the spin ground states of the charged quantum dot are optically coupled to excited trion states that exhibit nearly radiatively limited emission [27]. These properties have enabled post-selected spin-photon entanglement [28–31], spin-photon teleportation [32], and spin-spin entanglement [33], which are essential capabilities for quantum networks.

Quantum dots are also embedded in a high dielectric material that can be directly patterned to form nanophotonic cavities that enhance light-matter interactions [34–37]. Tremendous experimental progress has been made in the last decade using a quantum dot exciton strongly coupled to a nanophotonic cavity, including cavity reflectivity control [38], ultrafast optical switch [39–41], single photon level nonlinearities [42–44], non-classical light generation [45, 46], and spin-exciton quantum logic operations [47].

The effort to integrate quantum dot spins with cavities has also experienced rapid progress. Several works demonstrated deterministic loading of a spin in a quantum dot coupled to a nanophotonic cavity [48, 49], and more recently coherent control of the loaded spin [50] and spin-dependent Kerr rotation of photons [51, 52]. However, a coherent spin-photon quantum interface, the essential building block for quantum networks and distributed quantum computers, has not yet been realized.

In this thesis, we demonstrate a nanophotonic quantum interface for a single solid-state spin, and explore its applications in solid-state implementations of

quantum information processing. We utilize a strongly coupled quantum dot and photonic crystal cavity system. We show that this nanophotonic interface enables strong coherent spin-photon interactions, where a single solid-state spin can control the polarization of a photon, and a single photon can flip the spin state. We also show that this quantum interface allows deterministic generation of spin-photon entanglement, and optical spin readout with improved fidelity. Our work represents a critical step towards implementations of chip-integrated quantum networks and distributed quantum computers.

1.2 Quantum dots

Quantum dots are semiconductor nanocrystals that can confine charge carriers in a local potential trap with discretized energy levels. Although a single quantum dot contains tens of thousands of atoms, its optical properties are very similar to a single atom due to the quantum confinement of the charge carrier wavefunctions. Therefore we can effectively treat a quantum dot as a single atom with discrete energy levels in a theoretical model.

The quantum dots we study are self-assembled Indium Arsenide (InAs) nanocrystals confined in a Gallium Arsenide (GaAs) substrate. They are grown by molecular beam epitaxy based on Stranski-Krastanov method [53], and are provided by our collaborator, Dr. Glenn S. Solomon. The density of the quantum dots are typically $10 \sim 50\ \mu\text{m}^{-2}$.

1.2.1 Emission properties

A single quantum dot can occupy different quasi-particle states, such as neutral ground state, charge ground state, neutral exciton state, trion exciton state, biexciton state, dark exciton state and etc. Its exact energy level structures and associated emission properties can be very complicated, which are well explained in this excellent review paper found in Ref. [54] and are not within the scope of this thesis. Here we only consider the emission from the neutral and charged exciton states of a quantum dot.

The neutral exciton state is composed of a electron-hole pair, whereas the charged exciton state (referred as the trion state) contains another electron or hole, depending on whether the dot is negatively or positively charged. The electron-hole pair in both of these exciton states could radiatively recombine to the ground state with a quantum efficiency of $> 90\%$ in the cryogenic temperature [55, 56]. The radiative lifetime of quantum dot exciton is in the order of 1 ns [57]. But the linewidth of exciton transition are typically broadened to several GHz, due to dephasing [58], or spectral diffusion effects which could be caused by charge fluctuations [59, 60], thermal fluctuations [38], or nuclear spin noise [61, 62].

Different from real atoms, different quantum dots might emit at different frequencies and even with different polarizations, because their emission properties depend on their exact shape, size, strain, and local electric and magnetic fields. Figure 1.1 shows the typical photoluminescence spectrum of an ensemble of quantum dots in one of our wafers. Each sharp line in the spectrum roughly corresponds

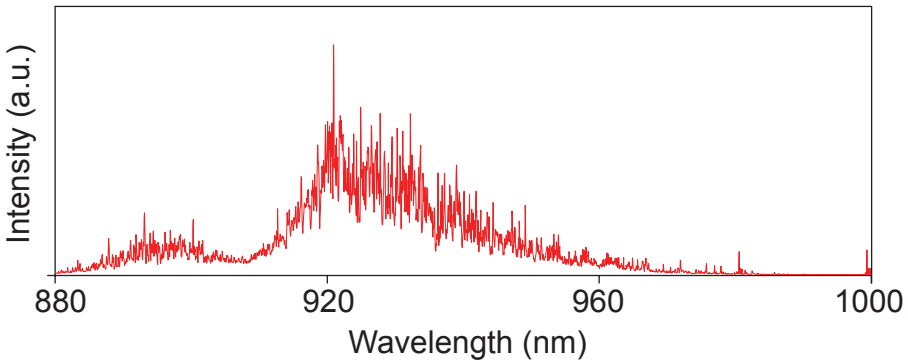

Figure 1.1: The spectrum of an ensemble of quantum dots in one of the typical wafers we used.

to the emission from a single quantum dot. The quantum dot ensembles show emission wavelength predominantly at $900 \sim 960$ nm, which is a very broad distribution compared to the linewidth of each individual quantum dot.

1.2.2 Charged quantum dots

In most of our reported experiments, we utilize a quantum dot that contains an extra electron, which has the spin degree of freedom that forms a stable qubit. Figure 1.2 shows the energy level structure of a negatively charged quantum dot containing a single electron. Positively charged dots would have a similar level structure. In both Fig. 1.2(a) and Fig. 1.2(b), we assume an external magnetic field is present to break the degeneracy of each energy level. The left panel shows the case where a magnetic field is parallel to the quantum dot growth direction (Faraday

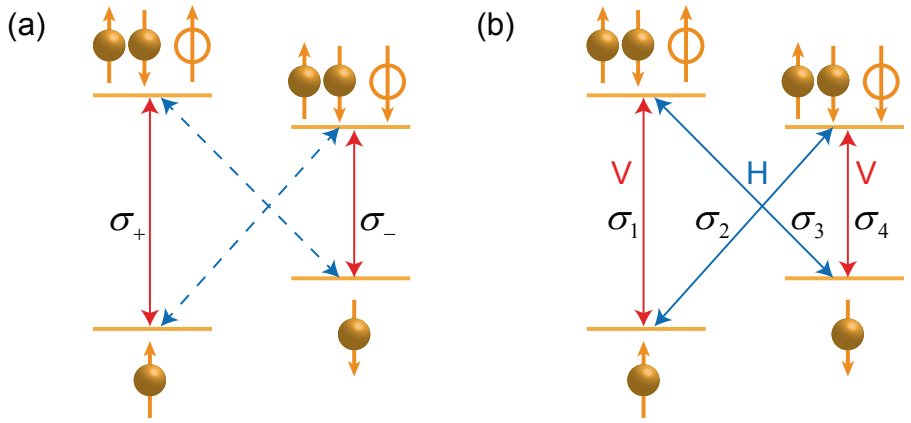

Figure 1.2: Energy level structure of a charged quantum dot in the presence of an external magnetic field. (a) The magnetic field is applied parallel to the quantum dot growth direction (Faraday configuration). (b) The magnetic field is applied perpendicular to the quantum dot growth direction (Voigt configuration).

geometry), whereas the right panel shows the case where a magnetic field is perpendicular to the quantum dot growth direction (Voigt geometry). The discussion in this section follows the excellent review paper found in Ref. [63].

In both configurations, the states of the quantum dot include two ground states, $|\uparrow\rangle$ and $|\downarrow\rangle$, corresponding to the electron spin that orients parallel and anti-parallel with the magnetic field respectively. They also contain two excited states that are consisted of an electron pair and a hole, denoted as $|\Uparrow\rangle$ and $|\Downarrow\rangle$, which are referred as the trion states. The trion states are two fold due to the two possible spin orientation of the hole.

In the Faraday configuration, only spin preserving transitions $|\Uparrow\rangle \leftrightarrow |\uparrow\rangle$ and $|\Downarrow\rangle \leftrightarrow |\downarrow\rangle$ are optically allowed, denoted as transition σ_+ and σ_- respectively. If

the quantum dot possesses ideal cylindrical symmetry, transition σ_+ and σ_- emits right- and left-circularly polarized light respectively. In the Voigt configuration, all four possible transitions are optically allowed, denoted as σ_1 - σ_4 respectively. Therefore the Voigt configuration supports two λ-systems, each is formed by one trion state and the two spin ground states. The vertical and cross transitions couple to orthogonal linear polarizations of light, denoted V and H, respectively. The exact orientations of V and H are determined by the shape and strain of the quantum dot.

1.2.3 Single qubit operations for a quantum dot spin

A complete set of single qubit operations include initialization, coherent manipulation, and readout of the qubit state [64]. Quantum dot spin qubits are optically coupled to trion states, which provides a mechanism to achieve all single qubit operations with optical pulses. Here we briefly review previous experimental developments on optical control of single quantum dot spins. Our discussion follows the review paper by K. De Greve et. al. [65].

1.2.3.1 Spin initialization

The presence of the λ-system in the Voigt configuration enables optical pumping of the spin into a particular spin ground states [66,67]. In a typical optical pumping experiment, a narrowband laser resonantly drives one branch of a λ-system, say transition σ_4. In this case, the population in the spin-up state is unperturbed. But

once the spin is in the spin-down state, it will be likely excited to the $|\Downarrow\rangle$ state, which will decay to both of the spin ground states with roughly equal probability. Therefore after a few cycles of optical excitation, any residual population in the spin-down state will be pumped into the spin-up state. In Voigt configuration, spin initialization can be completed within several nanoseconds, with fidelity exceeding 99.5% [66].

In the Faraday configuration, the idealized selection rules do not permit spin flips in the presence of an optical pumping field. However small imperfections in the selection rules can still lead to non-vanishing probabilities for the spin non-preserving transitions, which are exploited for optical pumping and spin initialization [68–70]. In the Faraday configuration, the spin initialization time is typically several hundreds of nanoseconds, with fidelity exceeding 99.8% [69].

1.2.3.2 Spin measurement

One typical approach for optical spin readout is to detect spin-dependent resonance fluorescence or absorption of the quantum dot upon optical pumping. In the Faraday configuration, the spin non-preserving transitions are weakly allowed. Therefore when a narrowband laser resonantly drives one optical transition (referred as the cycling transition), say transition σ_+, it generates many emitted photons from the same transition until the spin flips due to the imperfect selection rules. Both multi-shot [71, 72] and single-shot [73] spin readout has been demonstrated using this technique in the Faraday configuration. But the reported single-shot readout

fidelity is only $\sim 82\%$ [73], limited by the collection efficiency of the emitted photons and the imperfect cycling transitions. In the Faraday geometry, one can also optically measure the spin via the spin-dependent Kerr or Faraday rotation of a detuned laser [74–76]. However these experimental demonstrations did not reach the single-shot regime due to the small polarization rotation angles.

In the Voigt configuration, the quantum dot does not possess a cycling transition since all possible transitions are optically allowed. Therefore single-shot spin readout is not available by fluorescence light detection from a bare dot. This is actually one of the great challenge facing quantum information processing with quantum dot spin qubits. In Chapter 5 we will propose and demonstrate a new optical approach for spin readout by using a cavity QED system, which would make single-shot readout possible even for a quantum dot spin in the Voigt configuration. Multi-shot statistical spin readout has been demonstrated by using resonance fluorescence [23] or absorption [67] detection techniques.

1.2.3.3 Coherent spin manipulation

All the optical coherent spin manipulation experiments reported so far utilized a charged quantum dot in the Voigt configuration [21–26]. Due to the presence of the λ-system, a detuned broadband optical pulse could induce effective Rabi oscillations between two spin ground states. One can intuitively understand it through a stimulated Raman transition picture, where the broadband optical pulse contains many pairs of Raman sidebands which are in phase with each other, and each pair

of Raman sidebands effectively induce spin rotations by driving the two branches of a λ-system independently. The detuning between the center frequency of the optical pulse and the quantum dot transitions (any one of the four transitions) has to be large enough to minimize the undesired population in the excited trion states.

Since the quantum dot level structure contains two λ systems, one also need to make sure that the stimulated Raman transitions resulted from the two λ systems add constructively. Theories have shown that a circular-polarized optical pulse could lead to constructive interference between the two λ systems. Ref. [77] has provided a detailed description on the optical coherent spin rotation theory for a charged quantum dot.

The effective Rabi oscillations between two spin ground states demonstrate the ability to rotate the spin qubit by an arbitrary angle about a single axis. Full control of the spin qubit requires the ability to rotate the spin about a second axis, so that one can coherently prepare the spin into an arbitrary point in the Bloch sphere. The natural Larmor precession of the spin about the external magnetic field accomplishes this rotation. Previous experiments have demonstrated this ability using Ramsey interferometry measurements [23].

1.3 Photonic crystal cavities

Photonic crystals are periodic nanostructures fabricated on a dielectric material, which lead to periodic modulation of the refractive index in the length scale of an optical wavelength. In a photonic crystal, the motion of a photon obeys optical

Bragg scattering, very similarly as the way an electron propagates in a real crystal consisted of ionic lattices. In addition, one can engineer photonic crystals to open a photonic band gap, analogous to an electronic bandgap in semiconductors, which prohibits the propagation of photons for certain directions within some frequency range.

Defects in a photonic crystal can support highly localized cavity modes within the photonic band gap, referred as photonic crystal cavities. The properties of a photonic crystal cavity, such as the resonant frequency, quality factor, mode profile, and mode volume, can be easily controlled by tailoring the geometry of the photonic crystals or the shape of the defect areas. In addition, it is straightforward to integrate a photonic crystal cavity with other photonic structures using the photonic crystal architecture. For example, previous experiments have demonstrated coupled multiple cavities [78,79] and waveguide coupled photonic crystal cavities [40,80,81]. These assets make the photonic crystal cavity a very attractive platform for realizing integrated photonics.

1.3.1 Cavity design

Figure 1.3 shows the design of the photonic crystal cavity that we use in the reported experiments. The cavity design is based on a three-hole defect in a triangular 2D photonic crystal, referred as a L3 photonic crystal cavity. We also shift the inner three holes adjacent to the defect to optimize the quality factor [82]. In the design, we set the distance between the center of two adjacent holes a to be $a = 240$

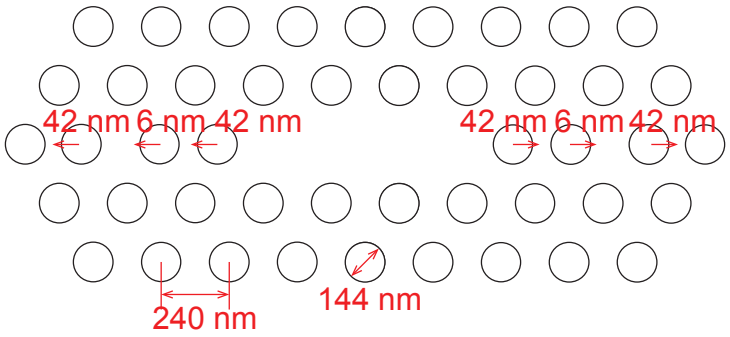

Figure 1.3: Illustration of the design of the L3 photonic crystal cavity.

nm, the radius of each hole to be $r = 72$ nm. The inner three holes adjacent to the defect are shifted outwards by 42 nm, 6 nm, and 42 nm respectively. Figure 1.4 shows the distribution of the x and y component of the electric field intensity and the total electric field intensity in the center plane of the photonic crystal slab for the cavity fundamental mode (the z-component of the electric field vanishes for the fundamental mode), calculated using the finite-difference time-domain (FDTD) method with a commercial software (Lumerical). The calculation shows that the cavity fundamental mode has a well-defined polarization axis that is along the $\hat{y}$ direction in the center region of the cavity.

The L3 photonic crystal cavity supports small mode volume and high quality factor, both of which are essential conditions for achieving strong light-matter interactions in the cavity. Using the FDTD method, we calculate the mode volume of the cavity to be $\sim 0.7(c/nf)^3$, where c is the speed of light, $n \simeq 3.6$ is the refractive index of GaAs, and f is the resonant frequency of the cavity. The effective volume of the cavity mode is even less than one wavelength cube. The cavity quality factor

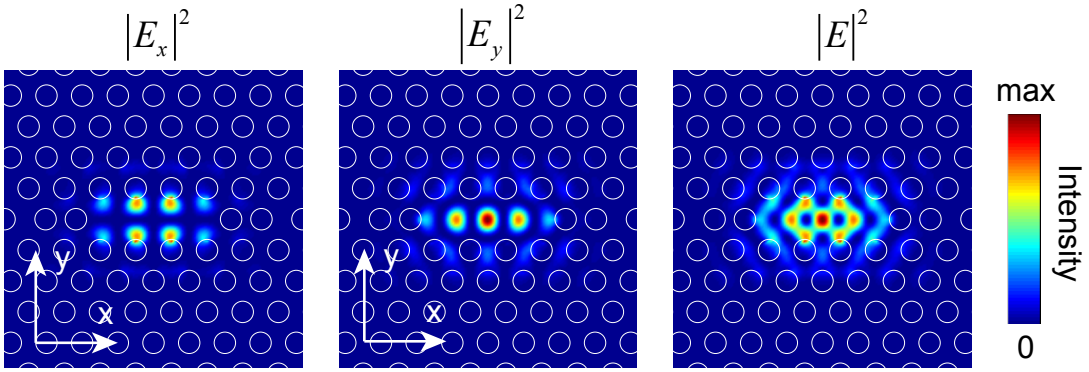

Figure 1.4: Calculated mode profile of the L3 photonic crystal cavity

is calculated to be $Q > 100,000$, but this value is difficult to achieve in experiments due to material absorptions and fabrication imperfections. In our measurements, we routinely attain a quality factor of $Q > 10,000$, which is already large enough to enable strong coupling between the photonic crystal cavity and an embedded quantum dot.

1.3.2 Device fabrication

Figure 1.5 shows a scanning electron microscope image of a typical fabricated cavity. We start the fabrication with a wafer that consists of a 160-nm-thick GaAs membrane. The membrane contains a single layer of InAs quantum dots at its center with a density of 10∼50 μm^{-2}. The membrane layer is grown on top of a 900-nm-thick $Al_{0.78}Ga_{0.22}As$ sacrificial layer. A distributed Bragg reflector composed of 10 layers of GaAs and AlAs is grown below the sacrificial layer and acts as a high reflective mirror. Photonic crystal structures are defined by electron beam lithography, followed by inductively coupled plasma dry etching and selective wet

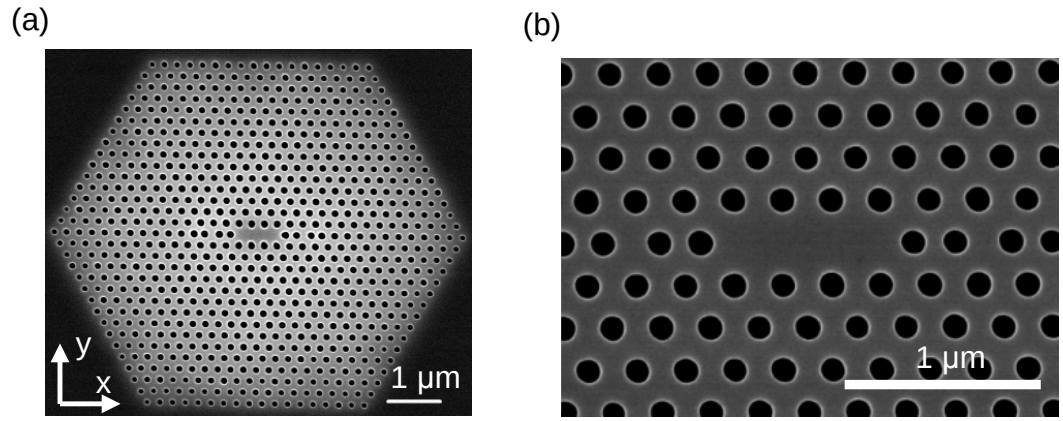

Figure 1.5: Scanning electron microscope image of a typical fabricated photonic crystal cavity device. (a) A full view of the device. (b) The zoom-in view showing the region of the cavity area.

etching of the sacrificial AlGaAs layer that creates a suspended membrane.

1.4 Outline of the thesis

Chapter 2 provides a theoretical background on using a cavity QED system to interface an optical active qubit with photons. In Chapter 3, we present experimental demonstrations of a spin-photon quantum switch, in which a single spin can control the polarization of a photon, and a single photon can flip the state of the spin. In Chapter 4, we discuss a theoretical proposal for deterministic generation of spin-photon entanglement, which is one of the most important applications of the spin-photon quantum switch, and represents an important step towards solid-state implementations of quantum repeaters and quantum networks. In Chapter 5, we show both theoretically and experimentally, a new method to optically read out

a quantum dot spin by using a cavity QED system. This new method achieves significant improvement in fidelity over typical approaches using fluorescence light detection.

All the experimental results reported in Chapter 3, 4, 5 will utilize a nanophotonic cavity QED system composed of a strongly coupled quantum dot and photonic crystal cavity. Chapter 6 reports our efforts to make this system more tunable and robust. In this chapter, we present a technique for tuning the frequency of a quantum dot that is strongly coupled to a photonic crystal cavity by applying strain. This tuning technique enables us to accurately control the detuning between a quantum dot and a cavity without affecting other emission properties of the dot, which is essential for lots of applications associated with cavity QED systems, including cavity reflectivity control [38], ultrafast optical switch [39–41], single photon level nonlinearities [42–44], non-classical light generation [45, 46], spin-exciton quantum logic operations [47], and our main focus, the spin-photon quantum interface. We conclude our work and discuss future research directions in Chapter 7.

Below we have listed all the relevant publications for each chapter.

Chapter 3:

Shuo Sun, Hyochul Kim, Glenn S. Solomon, and Edo Waks, A quantum phase switch between a single solid-state spin and a photon, *Nature Nanotechnology* 11, 539-544 (2016) [83].

Chapter 4:

Shuo Sun and Edo Waks, Deterministic generation of entanglement between

a quantum-dot spin and a photon, *Physical Review A* 90, 042322 (2014) [84].

Chapter 5:

Shuo Sun and Edo Waks, Single-shot optical readout of a quantum bit using cavity quantum electrodynamics, *Physical Review A* 94, 012307 (2016) [85].

Shuo Sun, Hyochul Kim, Glenn S. Solomon, and Edo Waks, Cavity enhanced optical readout of a single solid-state spin, *Manuscript in preparation.*

Chapter 6:

Shuo Sun, Hyochul Kim, Glenn S. Solomon, and Edo Waks, Strain tuning of a quantum dot strongly coupled to a photonic crystal cavity, *Applied Physics Letters* 103, 151102 (2013) [86].

Chapter 2: Interfacing an optical active qubit with photons using a cavity QED system

In this chapter, we provide theoretical background on using a cavity QED system to interface an optical active qubit with photons. We focus our analysis on a generic system consisted of an optical active qubit coupled to an optical cavity, as shown in Fig. 2.1(a). We assume that the qubit system has a λ-type energy structure as shown in Fig. 2.1(b), with two ground states that form a stable spin qubit, denoted as $|\uparrow\rangle$ and $|\downarrow\rangle$, and one excited state $|e\rangle$ that gives rise to spin-dependent optical transitions $\mu_\uparrow$ and $\mu_\downarrow$ respectively. The spin-dependent optical transitions provide a mechanism to interconnect the spin qubit with photons. This energy structure exists in many qubit systems that are optically addressable, such as cold atoms, trapped ions, charged quantum dots and color centers, and therefore represents a generic model.

In order to induce strong spin-photon interactions, we selectively couple the optical transition $\mu_\uparrow$ to a cavity mode, while decouple the other transition $\mu_\downarrow$ to the cavity, either by a large detuning or by selection rules if transition $\mu_\downarrow$ emits a photon with a different polarization than the cavity mode. In this configuration the coupling between the atom and cavity depends on the spin state. The cavity thus

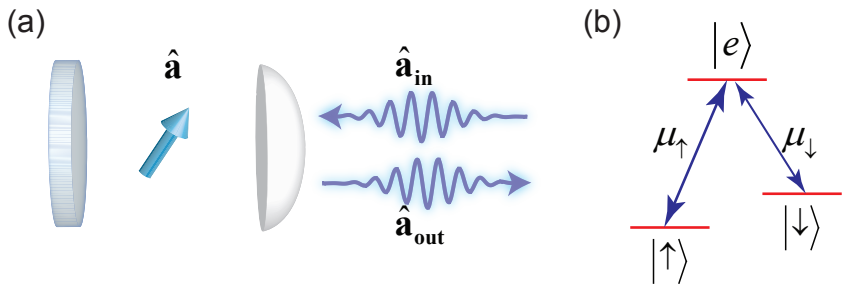

Figure 2.1: Theoretical model for a generic cavity QED system composed of an optical active qubit coupled to an optical cavity. (a) A schematic cavity QED system. (b) Energy level structure of a generic optical active qubit system.

exhibits spin-dependent reflection or transmission coefficients, enabling control of a reflected or transmitted photon by the spin qubit. In our model, we assume that the cavity field only couples to its reflective mode without loss of generality. In this case the spin only modulates the reflection coefficient of the cavity. Double-sided cavities would work similarly with minor modifications.

This chapter is organized as follows. Section 2.1 calculates the spin-dependent cavity reflection coefficients. Section 2.2, we show that we can realize a quantum switch between the spin qubit and a photonic qubit by utilizing the spin-dependent cavity reflection coefficient. The realization of a spin-photon quantum switch requires the incident photon to be resonant with both the cavity mode and the transition $\mu_{\uparrow}$. In Section 2.3 reviews possible applications by detuning the photon or transition $\mu_{\uparrow}$ from the cavity mode.

2.1 Calculation of spin-dependent cavity reflection coefficients

We calculate the cavity reflection coefficients using cavity input-output formalism [87]. We define $\hat{\mathbf{a}}$ as the bosonic annihilation operator for the cavity field, and $\hat{\mathbf{a}}_{\mathbf{in}}$ and $\hat{\mathbf{a}}_{\mathbf{out}}$ as the operators for the cavity coupled incidence and reflection modes. These operators are related by the cavity input-output relation

$$\hat{\mathbf{a}}_{\mathbf{out}} = \hat{\mathbf{a}}_{\mathbf{in}} - \sqrt{\kappa_{ex}}\hat{\mathbf{a}}, \tag{2.1}$$

where κ_{ex} is the cavity energy decay rate to the reflection mode of the cavity.

In order to calculate the reflection coefficients, we need an expression for the cavity field operator $\hat{\mathbf{a}}$. We assume that the incident photon is monochromatic with a frequency of ω. We express the Hamiltonian for the coupled atom and cavity system in the rotating reference frame with respect to ω, given by

$$\mathbf{H} = \hbar(\omega_c - \omega)\hat{\mathbf{a}}^\dagger\hat{\mathbf{a}} + \hbar(\omega_x - \omega)\hat{\sigma}_-^\dagger\hat{\sigma}_- + ig\hbar(\hat{\mathbf{a}}\hat{\sigma}_-^\dagger - \hat{\sigma}_-\hat{\mathbf{a}}^\dagger), \tag{2.2}$$

where $\hat{\sigma}_-$ is the lowering operator for transition $\mu_\uparrow$, ω_c and ω_x are the resonance frequencies of the cavity mode and transition $\mu_\uparrow$ respectively, and g is the coupling strength between the cavity mode and transition $\mu_\uparrow$. In the weak field limit, the Heisenberg-Langevin equations are [14, 88, 89]

$$\frac{d\hat{\mathbf{a}}}{dt} = -\big[i(\omega_c - \omega) + \frac{\kappa}{2}\big]\hat{\mathbf{a}} - ig\hat{\sigma}_- + \sqrt{\kappa_{ex}}\hat{\mathbf{a}}_{\mathbf{in}} \tag{2.3}$$

$$\frac{d\hat{\sigma}_-}{dt} = -\big[i(\omega_x - \omega) + \gamma\big]\hat{\sigma}_- - ig\hat{\mathbf{a}}, \tag{2.4}$$

where κ is the total cavity energy delay rate given by $\kappa = \kappa_{ex} + \kappa_i$, κ_i is the intrinsic loss rate of the cavity due to material absorption and coupling to undesired leaky modes, and γ is the dipole decay rate of for transition $\mu_\uparrow$.

We calculate the cavity field operator by taking the steady solution of Eq. 2.3 and Eq. 2.4. When the spin is in spin-down state, we have $\langle\hat{\sigma}_{-}\rangle = 0$, therefore the steady solution for $\hat{\mathbf{a}}$ can be calculated from Eq. 2.3 and is given by

$$\hat{\mathbf{a}} = \frac{\sqrt{\kappa_{ex}}\hat{\mathbf{a}}_{\mathbf{in}}}{i(\omega_c - \omega) + \frac{\kappa}{2}}. \tag{2.5}$$

When the spin is in spin-up state, the expression for $\hat{\mathbf{a}}$ is given by

$$\hat{\mathbf{a}} = \frac{\sqrt{\kappa_{ex}}\big[i(\omega_x - \omega) + \gamma\big]}{\big[i(\omega_c - \omega) + \frac{\kappa}{2}\big]\big[i(\omega_x - \omega) + \gamma\big] + g^2}\hat{\mathbf{a}}_{\mathbf{in}}. \tag{2.6}$$

We calculate the cavity reflection coefficients $r_{\downarrow}$ and $r_{\uparrow}$ for both the spin-down and spin-up cases by combining Eq. 2.5 or Eq. 2.6 with Eq. 2.1. For the spin-down case, we obtain $\hat{\mathbf{a}}_{\mathbf{out}} = r_{\downarrow}\hat{\mathbf{a}}_{\mathbf{in}}$, where $r_{\downarrow}$ is given by,

$$r_{\downarrow} = 1 - \frac{\alpha\kappa}{i(\omega_c - \omega) + \frac{\kappa}{2}}, \tag{2.7}$$

where α is the interference contrast given by $\alpha = \kappa_{ex}/\kappa$. For the spin-up case, we obtain $\hat{\mathbf{a}}_{\mathbf{out}} = r_{\uparrow}\hat{\mathbf{a}}_{\mathbf{in}}$, where $r_{\uparrow}$ is given by

$$r_{\uparrow} = 1 - \frac{\alpha\kappa\big[i(\omega_x - \omega) + \gamma\big]}{\big[i(\omega_c - \omega) + \frac{\kappa}{2}\big]\big[i(\omega_x - \omega) + \gamma\big] + g^2}. \tag{2.8}$$

2.2 Resonance case: a spin-photon quantum switch

We focus on the resonance condition where $\omega = \omega_c = \omega_x$. In this case, the cavity reflection coefficients simplify to

$$r_{\downarrow} = 1 - 2\alpha \tag{2.9}$$

$$r_{\uparrow} = 1 - \frac{2\alpha}{1 + C}, \tag{2.10}$$

where C is the cooperativity of the system given by $C = 2g^2/\kappa\gamma$.

When $\alpha > 0.5$ and $C > 2\alpha - 1$, $r_\uparrow$ and $r_\downarrow$ have opposite signs. Thus, the spin state conditionally shifts the phase of a reflected photon by π, implementing a quantum phase operation. An ideal phase switch would be attained in the limit of large cooperativity ($C \gg 1$) and a perfect single-sided cavity ($\alpha = 1$) where the reflection coefficient becomes $r_\downarrow = -1$ and $r_\uparrow = 1$.

The quantum phase switch allows one qubit to conditionally switch the other qubit between its two orthogonal eigenstates. We consider the case where the polarization state of the photon encodes quantum information. We assume that the cavity mode has a well defined polarization direction $\hat{y}$. Therefore only a y-polarized photon experiences spin-dependent phase shift upon reflection, whereas an x-polarized incident photon does not couple to the cavity and gets directly reflected without a phase shift. If the cavity mode does not have a well-defined polarization (i.e. the cavity supports polarization degenerate modes), we could use a simple polarization interferometry setup as illustrated in Fig. 2.2 to implement the similar idea.

We express the state of a photon incident on the cavity in the basis states $|x\rangle$ and $|y\rangle$, which denote the polarization states oriented orthogonal and parallel to the cavity mode respectively. For a right-circularly-polarized incident photon $|x\rangle + i|y\rangle$, the reflected state is given by $|x\rangle + ir_{\uparrow(\downarrow)}|y\rangle$ (before renormalization). In the limit of large cooperativity and perfect single-sided cavity, the state of the reflected photon remains right-circularly polarized if the atom is in the spin-up state, but becomes left-circularly polarized for spin-down. Similarly, a single control photon can flip the state of the spin. If the spin is prepared in the state $|\uparrow\rangle + |\downarrow\rangle$, then after a

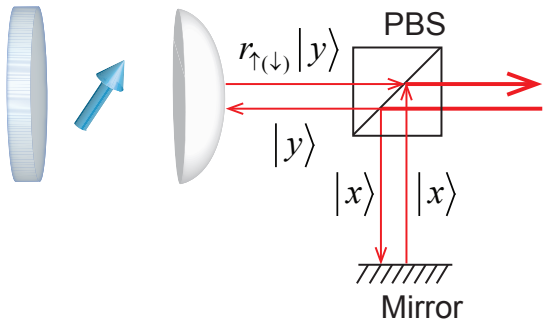

Figure 2.2: Schematic setup to implement a spin-photon quantum switch where the polarization states of the photon encode quantum information.

y-polarized photon reflects from the cavity the spin-state transforms to $|\uparrow\rangle - |\downarrow\rangle$, but an x-polarized photon does not flip the spin.

We note that when $\alpha > 0.5$ but $C < 2\alpha - 1$, $r_\uparrow$ and $r_\downarrow$ have the same sign. Thus the quantum phase operation is not available for a resonant photon if the system cooperativity is too low.

2.3 Detuned case: spin-dependent Kerr rotation

The general expression for $r_\downarrow$ and $r_\uparrow$ are given by Eq. 2.7 and Eq. 2.8 respectively. We can rewrite $r_{\downarrow(\uparrow)}$ as $r_{\downarrow(\uparrow)} = |r_{\downarrow(\uparrow)}|e^{i\phi_{\downarrow(\uparrow)}}$, where $\phi_{\downarrow(\uparrow)}$ represents the phase of the reflection coefficient $r_{\downarrow(\uparrow)}$. Since in general $\phi_\downarrow \neq \phi_\uparrow$, the spin can still apply spin-dependent phase shift on the photon. The phase difference between the spin-up and spin-down state ϕ is given by $\phi = \phi_\downarrow - \phi_\uparrow$, which is typically nonzero but not necessarily π any more.

The nonzero value of ϕ can be utilized to realize spin-dependent Kerr rotation

of a photon, as demonstrated in Ref. [51, 52]. Assuming the polarization of the incident photon is in the state $|x\rangle + i|y\rangle$, the reflected state becomes $|P_{\uparrow(\downarrow)}\rangle = |x\rangle + i|r_{\uparrow(\downarrow)}|e^{i\phi_{\uparrow(\downarrow)}}|y\rangle$ (before renormalization). Therefore, the polarizations of the reflected photon are different for the spin-up and spin-down cases, as long as $\langle P_\uparrow|P_\downarrow\rangle \neq 1$, which is equivalent to $\phi \neq 0$.

Similarly, a single detuned photon can also rotate the state of the spin. If the spin is prepared in the state $|\uparrow\rangle + |\downarrow\rangle$, then after a y-polarized photon reflects from the cavity the spin-state transforms to $|r_\uparrow||\uparrow\rangle + |r_\downarrow|e^{i\phi}|\downarrow\rangle$ (after taking out an overall phase factor). If $|r_\uparrow| \simeq |r_\uparrow|$, this operation corresponds to the rotation of the spin Bloch vector by an angle ϕ along the equator of the spin Bloch sphere.

For the detuned case, we do not require the cooperativity to be greater than $2\alpha - 1$ in order to induce spin-dependent phase shift. Indeed Ref. [51] demonstrated spin-dependent Kerr rotation of a photon with a coopeartivity of $C = 0.2$. However, there is still significant difference between the regime $C > 2\alpha - 1$ and $C < 2\alpha - 1$. Figure 2.3 shows numerically calculated phase shift ϕ as a function of the detuning Δ_c and Δ_x, where we define $\Delta_c = \omega - \omega_c$ and $\Delta_x = \omega - \omega_x$. In both Fig. 2.3(a) and Fig. 2.3(b), we use the following parameters from a realistic quantum dot based cavity QED system [83]: $\alpha = 0.8$, $\kappa/2\pi = 36$ GHz, $\gamma/2\pi = 3$ GHz. Figure 2.3(a) shows the case where we set $g/2\pi = 10.4$ GHz so that the cooperativity is $C = 2$, and Fig. 2.3(b) shows the case where we set $g/2\pi = 3.3$ GHz so that the cooperativity is $C = 0.2$. When the cooperativity is large, we are able to tune the phase shift ϕ to an arbitrary value between $-\pi$ and π, by simply controlling the detuning Δ_c and Δ_x. However, when the cooperativity is small, we can only tune the phase shift ϕ

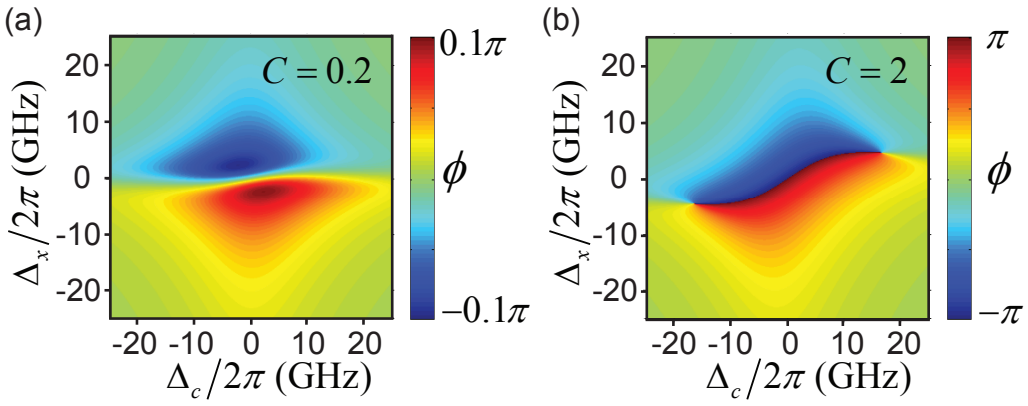

Figure 2.3: Phase shift ϕ as a function of the detuning Δ_c and Δ_x. (a) $C = 0.2$. (b) $C = 2$.

between $-\phi_{max}$ and ϕ_{max}, where $\phi_{max} < \pi$ is an upper limit that is determined by the system cooperativity. As an example, in Fig. 2.3(a) we have $\phi_{max} = 0.1\pi$.

Chapter 3: Cavity assisted spin-photon quantum switch

In this chapter, we discuss experimental demonstrations of a spin-photon quantum switch using a strongly coupled charged quantum dot and a photonic crystal cavity. Before this work, our group has demonstrated a quantum controlled-not gate between a quantum dot exciton qubit and a photon [47]. But the quantum exciton states have short lifetimes that make them impractical for quantum information processing applications.

The energy levels of a charged quantum dot in the Voigt configuration is shown in Fig. 1.2(b), which consists of two λ-systems and is slightly different from the single λ-system described in Chapter 2. However, we can still induce spin-dependent cavity reflectivity by resonantly coupling only transition σ_1 with the cavity mode, and decoupling all other transitions from the cavity by a large magnetic field induced detuning. Thus, the quantum dot resonantly couples to the cavity only when it is in the spin-up state, inducing a spin-dependent reflection coefficient. As described in Section 2.2, we are able to realize a quantum switch by utilizing the spin-dependent reflection coefficients.

This chapter is organized as follows. Section 3.1 discusses device characterization. In Section 3.2, we report spin-dependent cavity reflectivity. In Section 3.3 and

Section 3.4, we demonstrate control of a reflected photon by coherently manipulating the spin, and control of the spin state with a single photon respectively. Section 3.5 concludes the discussions of this Chapter.

3.1 Device characterization

To characterize the device, we mount the sample in a closed-cycle liquid-helium cryostat and cool it down to 3.6 K. The sample mount is placed inside the bore of a superconducting magnet that can apply magnetic fields up to 9.2 T. The sample is oriented such that the magnetic field is in the in-plane direction (Voigt configuration), and the cavity axis is approximately 45 degree with respect to the magnetic field. Sample excitation and collection is performed with a confocal microscope using an objective lens with numerical aperture of 0.68. The coupling efficiency for this configuration is measured to be 1% by measuring the Stark shift of the quantum dot under cavity-resonant excitation [90].

We identify a charged quantum dot coupled to the cavity from the photoluminescence spectrum of the device under a magnetic field applied in the Voigt configuration. Fig. 3.1(a) shows the photoluminescence spectrum from the device used in our measurements when excited using an 860 nm continuous wave laser. At 0 T, the emission spectrum shows a bright peak due to the cavity (labeled as CM) and a second peak due to the quantum dot (labeled as QD), which is red-detuned from the cavity resonance by 0.19 nm (67 GHz). As we increase the magnetic field, the quantum dot splits into four peaks corresponding to the four optical transitions

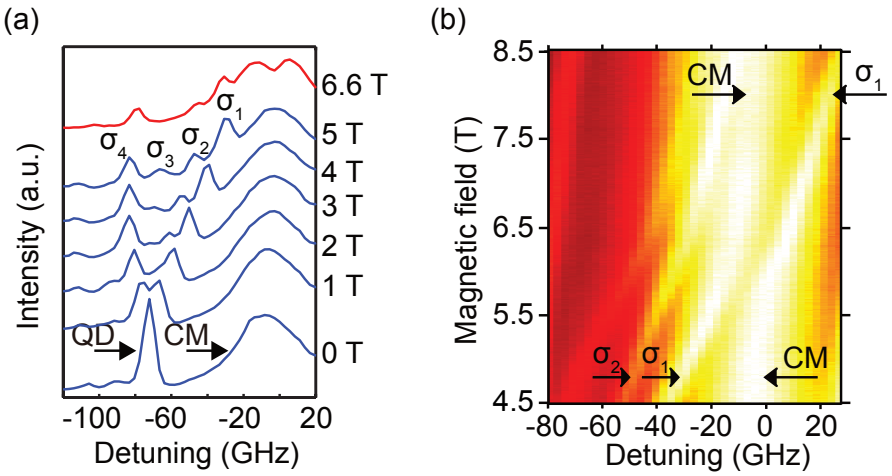

Figure 3.1: Device characterization with photoluminescence. (a) Photoluminescence spectrum. The blue lines show the spectra at various magnetic fields ranging from 0 T to 5 T. The red line shows the spectrum at 6.6 T, where transition σ_1 is resonant with the cavity. (b) Cavity photoluminescence as a function of the magnetic field.

shown in Fig. 1.2(b).

To demonstrate strong coupling between the quantum dot and the cavity, we finely tune the magnetic field over the range of 4.5 T to 8.5 T and measure the cavity photoluminescence. Fig. 3.1(b) shows the photoluminescence spectrum near the cavity resonance as a function of magnetic field. In this range, transition σ_1 tunes over the cavity resonance and exhibits an anti-crossing, indicating that the system operates in the strong coupling regime.

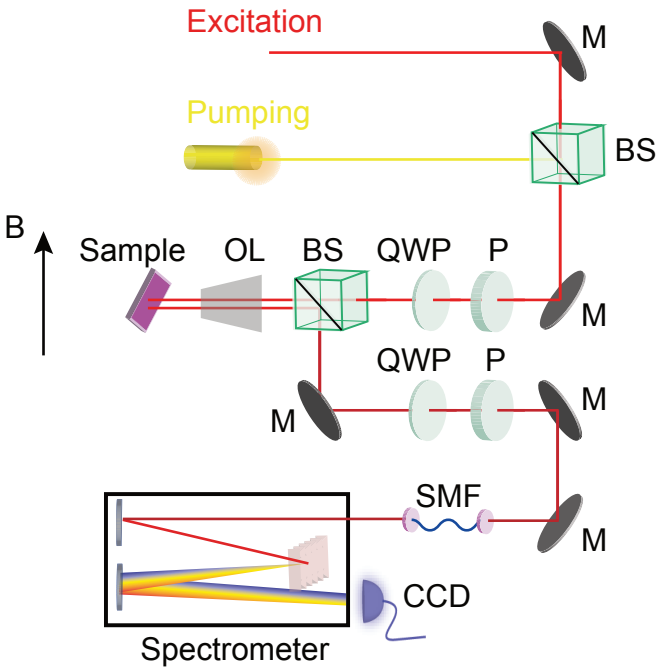

Figure 3.2: Measurement setup. OL, objective lens; QWP, quarter wave plate; P, polarizer; BS, beam splitter; M, mirror; SMF, single mode fiber; CCD, charged coupled device.

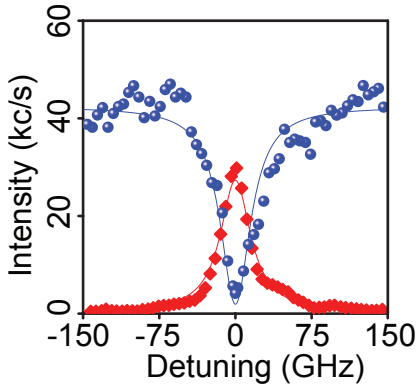

Figure 3.3: Co-polarized (blue circles) and cross-polarized (red diamonds) cavity reflection spectrum with no magnetic field. Blue and red solid lines show the calculated spectrum.

3.2 Spin-dependent cavity reflectivity

To demonstrate that the spin can flip the state of the photon, we use the polarization interferometry set-up shown in Fig. 3.2. We excite the cavity with right-circularly polarized light, and measure the reflected signal along either the left-circularly or right-circularly polarized component. Fig. 3.3 shows both the cross-polarized (red diamonds) and co-polarized reflection spectrum (blue circles) when the quantum dot is detuned from the cavity so that the two systems are decoupled. By fitting the reflection spectrum to a Lorentzian lineshape (blue and red solid lines), we determine the cavity energy decay rate to be $\kappa/2\pi = (35.9 \pm 0.7)$ GHz and the interference contrast to be $\alpha/2\pi = 0.81 \pm 0.01$.

We next apply a magnetic field of 6.6 T that tunes transition σ_1 onto cavity resonance via a Zeeman shift. We excite the quantum dot with a narrowband tunable laser to optically pump the spin state [66, 67]. We first tune the optical pumping laser to transition σ_4 to prepare the quantum dot in the spin-up state. The blue circles in Fig. 3.4(a) show the cross-polarized reflection spectrum with the optical pumping laser, which exhibits a vacuum Rabi splitting. When we turn off the pumping laser, we observe a reduced contrast due to random spin fluctuations (red diamonds). In contrast, when we optically pump transition σ_2 to initialize the quantum dot to the spin-down state, we observe a spectrum that closely resembles a bare cavity (Fig. 3.4(b)). This spin-dependent reflection spectrum is one of the essential properties of the phase switch.

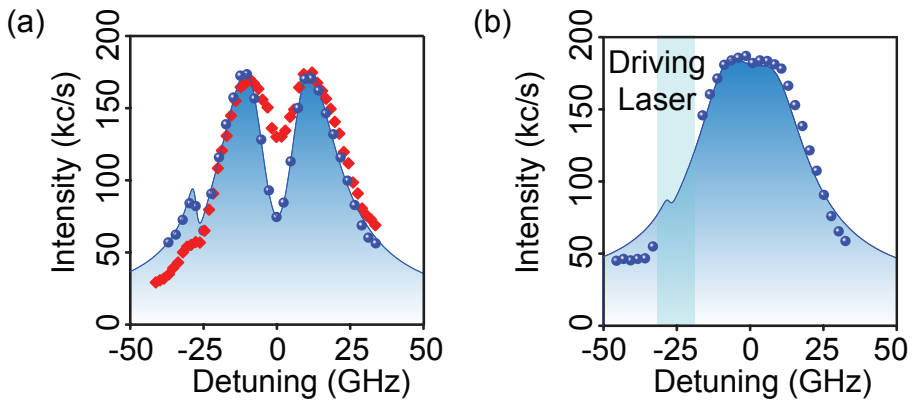

Figure 3.4: Spin-dependent cavity reflectivity. (a) Cavity reflection spectrum under a 6.6 T magnetic field with (blue circles) and without (red diamonds) an optical pumping laser resonant with transition σ_4. The blue solid line shows the calculated spectrum for the case where the optical pumping laser is turned on. With the pumping laser, we observe a suppression of the cavity response at the σ_1 resonance due to strong coupling. We also observe a Fano-resonant lineshape at 27 GHz detuning, corresponding to the coupling between transition σ_2 and the cavity mode. (b) Cavity reflection spectrum when the pump laser is resonant with transition σ_2. The blue circles show the measured spectrum, and the solid line shows calculated spectrum. The center wavelength is 927.48 nm for all panels.

3.3 Coherent control of cavity reflectivity

To demonstrate control of a reflected photon using a coherently prepared spin state, we use all-optical coherent control to manipulate the spin. We fix the magnetic field at 6.6 T. A narrowband continuous-wave laser tuned to transition σ_4 performs spin initialization and circularly polarized picosecond optical pulses generate an effective spin rotation [22, 23]. We perform spin rotations using 6 ps rotation pulses with center frequencies detuned by 520 GHz from the cavity resonance (equal to 15 cavity linewidth). To rotate the spin over the Bloch sphere, we utilize the Ramsey interferometry setup illustrated in Fig. 3.5(a), which generates a pair of rotation pulses separated by a time delay τ. A third laser pulse probes the cavity reflectivity a time Δt after the second rotation pulse. We attenuate this laser so that a single pulse contains an average of 0.12 photons coupled to the cavity to ensure a low probability of two-photon events. We set the power of the continuous-wave optical pumping laser to 30 nW. At this power we measure a spin initialization time of (1.27 ± 0.09) ns, which is slow compared with τ and Δt, but fast compared with the repetition time of the experiment (13 ns).

Fig. 3.5(b) shows the reflected probe intensity as a function of rotation pulse power P and delay τ, where we set Δt to 140 ps. We observe Ramsey oscillations in the reflected probe intensity as a function of both P and τ. Fig. 3.5(c) plots the emission intensity of the quantum dot at transition σ_2 for the same measurement, which provides a second readout of the spin state. We observe the same Ramsey oscillation pattern in the quantum dot emission signal, confirming that the

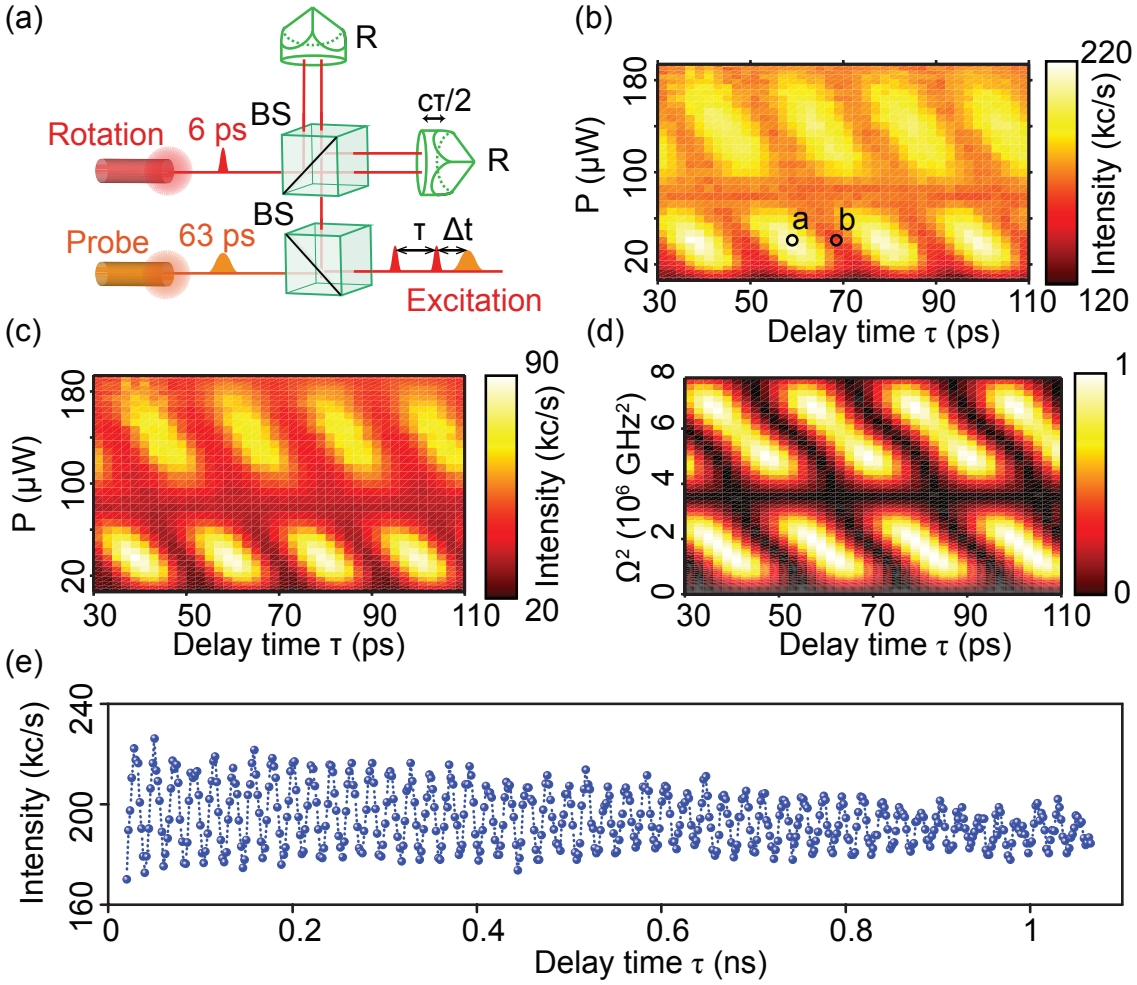

Figure 3.5: Ramsey interference measurements. (a) Experimental setup for generating the Ramsey pulse sequence. The delay time τ between the two rotation pulses is controlled by a movable retro-reflector mounted on a computer-controlled translation stage. BS, beam splitter; R, retro-reflector. (b) Reflected probe intensity as a function of rotation pulse power P and the delay time τ. (c) Intensity of the quantum dot emission at σ_2 transition frequency as a function of rotation pulse power P and the delay time τ. (d) Calculated spin-down state population as a function of peak rotation pulse power and the delay time τ. We express the rotation pulse as a classical time-varying Rabi frequency with a Gaussian pulse shape and peak power Ω^2. (e) Reflected probe intensity as a function of delay time τ.

reflection modulation shown in Fig. 3.5(b) is induced by coherent spin manipulation. Fig. 3.5(d) shows the numerically calculated value for the population of the spin-down state for comparison, which exhibit good agreement with experiments.

In Fig. 3.5(e) we plot the reflected probe intensity over a larger time range of 1 ns. We fix the power of each rotation pulse to 40 μW, which corresponds to a $\pi/2$-rotation. From the decay of the fringe visibility, we calculate a $T_2^\star$ time of (0.94 ± 0.02) ns. This coherence time is limited by inhomogeneous broadening due to a slowly fluctuating nuclear spin background [20], along with decoherence due to continuous optical pumping during the rotation pulse sequence. We could reduce these effects by turning off the pump laser during the measurement process and using a nuclear field locking [20] or spin echo technique [21], which has been shown to improve the coherence to up to 2.6 μs.

To characterize the fidelity of the spin state preparation, we tune the probe laser across the cavity resonance while setting P and τ to the conditions indicated by the circles in Fig. 3.5(b). The resulting cavity spectra are plotted in Fig. 3.6. In Fig. 3.6(a) the two pulses arrive in-phase with the Larmor precession of the spin, and the quantum dot rotates to the spin-down state. The cavity spectrum (blue circles) is thus similar to the bare cavity Lorentzian lineshape. Figure 3.6(b) shows the case where the two rotation pulses arrive out-of-phase and the quantum dot rotates back to the spin-up state. The cavity (blue circles) now exhibits a strongly coupled spectrum. We also plot the measured spectrum when $\Delta t = 13$ ns (red diamonds) for comparison. At this condition the spin is re-initialized to the spin-up state in both cases.

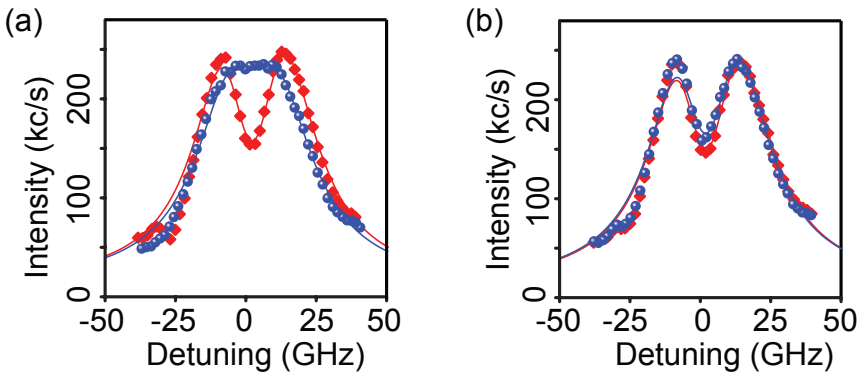

Figure 3.6: Time-resolved cavity reflection spectrum. (a) and (b), Reflected probe intensity as a function of probe detuning at the rotation condition indicated by point a and point b in Fig. 3.5(b) respectively. Blue circles are $\Delta t = 140$ ps; red diamonds are $\Delta t = 13$ ns. Solid lines are the calculated spectra. The center wavelength is 927.48 nm for both spectra.

We numerically fit the data to a model. From the fit we determine the spin preparation fidelity in these two conditions to be 0.70 ± 0.04 and 0.74 ± 0.05. The imperfect population transfer could be caused by a number of factors such as re-initialization of the spin by optical pumping during the interval between the rotation and the probe pulse, and decoherence due to power-induced trion dephasing caused by the rotation pulses [23, 91].

3.4 Controlling a spin with a photon

The previous measurements demonstrate that the spin state of the quantum dot induces a conditional phase shift on the photon. A quantum phase switch would also exhibit the complementary effect, where reflection of a single photon rotates the spin state. To demonstrate this phase shift, we use the experimental configuration

shown in Fig. 3.7(a). We again perform a Ramsey interference measurement but we inject a weak laser pulse that serves as the control field before the second rotation pulse. We generate the control pulse in the same way as the probe pulse in the previous measurement, with pulse duration of 63 ps. When a control photon couples to the cavity, it imposes a phase shift on the spin-down state, which shifts the phase of the Ramsey fringes.

We perform spin readout by monitoring the emission at the σ_2 frequency. The blue circles in Fig. 3.7(b) show the occupation probability of the spin-down state conditioned on the detection of a control photon, as a function of delay between the two rotation pulses. These data are obtained by performing a two photon correlation measurement. The blue solid line is a numerical fit to a sinusoidal function. We compare this curve to the occupation probability of the spin-down state when we block the control field (black squares with black line as a numerical fit). The interference fringe conditioned on detecting a single control photon is shifted in phase by $(1.09 \pm 0.09)\pi$ radians relative to the case where there is no control photon, demonstrating that a single control photon applies a large phase shift to the spin. We attribute the degraded visibility of the Ramsey fringe conditioned on a control photon to finite cooperativity, intrinsic cavity losses and occasional two-photon incidence events.

We can tune the phase shift imparted on the spin by a control photon by introducing a frequency detuning between the control field and transition σ_1, which enables us to apply arbitrary controlled phase shifts. Fig. 3.7(c) shows the same measurement for a blue detuned control field. The conditioned data (blue circles)

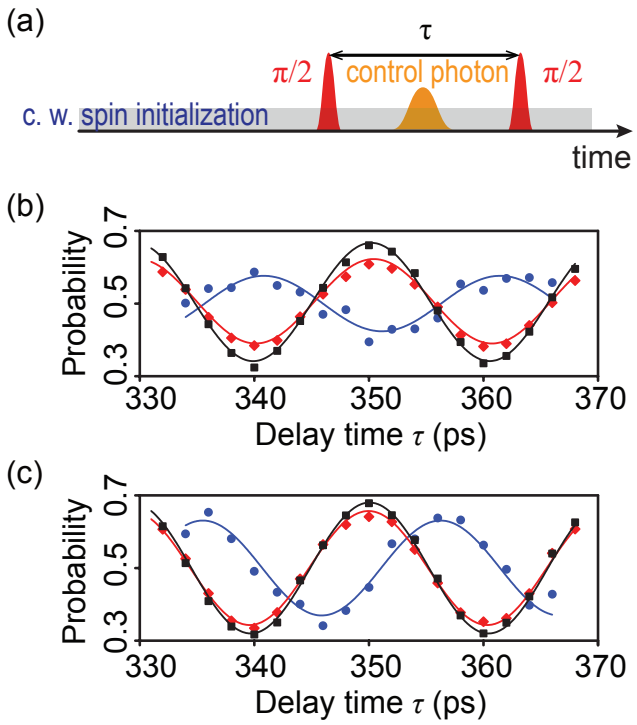

Figure 3.7: Photon-induced spin phase switch. (a) Pulse timing diagram showing the relative time delays between the rotation pulses and the control field. (b) Occupation probability of the spin-down state as a function of the delay time τ, in the absence of control pulse (black squares), conditioned on detecting a reflected control photon polarized along the cavity axis (blue circles), and in the presence of the control field but not conditioning on the detection of a control photon (red diamonds). The control field is resonant with the σ_1 quantum dot transition. (c) Same as (b), except that the control field is blue detuned from the σ_1 quantum dot transition.

show a $(0.59 \pm 0.05)\pi$ radian phase shift, which corresponds to a detuning of 7.3 GHz. We also plot the occupation probability of the spin-down state in the presence of the control field but without conditioning on the detection of the control photon (red diamonds in Fig. 3.7(b)(c)). These curves are very similar to the case where the control field is blocked, which indicates that the average number of control photons per pulse coupled to the cavity is much smaller than one.

3.5 Discussions

We have demonstrated a solid-state spin-photon quantum phase switch, which is the fundamental building block for numerous applications including entanglement distribution [4, 5], non-destructive qubit measurements [6–8], and strong photon-photon interactions for photonic quantum computation [9,10]. The high light-matter coupling strength of our solid-state devices enables a phase switch operating at unprecedented bandwidths, where the spin can switch photon wavepackets as short as 63 ps. Perhaps the most intriguing aspect of our quantum switch is that it monolithically combines spins with strongly interacting nanophotonic structures on a single semiconductor chip, which may have many beneficial properties for future integration and scalability.

Chapter 4: Deterministic generation of spin-photon entanglement

One important application of the spin-photon quantum switch is to deterministically generate entanglement between the quantum dot spin and a photon. Entangling quantum dot spin with a flying photon could enable photon mediated entanglement between spatially separated quantum dot spin qubits [14, 92] as well as other matter qubits [93] for creating hybrid quantum systems. These capabilities could ultimately lead to realization of long distance quantum networks [1, 2] and distributive quantum computation [3].

Several groups have reported entanglement between a quantum dot spin and a single photon [28–31]. These milestone achievements were attained by utilizing spontaneous emission of an excited quantum dot. The polarization state of the emitted photon was entangled with the spin state of the quantum dot by optical selection rules. However, because the two spin states in these experiments were non-degenerate, the emission frequency of the photon retained which-path information of the spin state. To eliminate this which-path information, fast time-domain detection was required. This operation can be understood as a post selection of photons arriving in a time period that is short compared to the frequency mismatch between the two spin-dependent optical transitions. However, post-selection leads

to probabilistic entanglement with low success probability.

One method to eliminate post-selection is to utilize a spin-dependent elastic scattering process, instead of inelastic scattering, to avoid entangling spin with the photon energy. Several such approaches have been proposed using strong interactions between a quantum dot and a cavity [16,94–96]. However, all of these methods require the cavity to support two degenerate polarization modes, and the quantum dot spin states to be degenerate. Although cavities with degenerate polarization modes can be designed theoretically [97], the degeneracy is usually broken in real devices due to fabrication imperfections, and complex steps are usually required to restore the cavity mode degeneracy [98–100]. More importantly, all-optical coherent control typically requires a strong in-plane magnetic field to break the selection rules [21–26], which also breaks the degeneracy of the spin transitions.

Here, we propose and analyze a protocol for deterministic generation of entanglement between the spin state of a quantum dot and the polarization state of a photon using elastic scattering in a cavity QED system. The proposal is based on the spin-photon quantum switch that we have demonstrated in Chapter 3. It requires coupling between only one non-degenerate quantum dot spin transition and a single cavity mode. We analyze the performance of the protocol and show that it can attain high entanglement fidelity for a realistic coupled quantum dot - nanophotonic cavity system. Our protocol could serve as an important building block for quantum networks and chip-integrated quantum devices.

This chapter is organized as follows. Section 4.1 describes the proposed protocol. In Section 4.2, we derive an analytical expression for the entanglement fidelity,

which acts as a measure of the quality of the generated entanglement. In Section 4.3, we study the system fidelity under realistic experimental conditions. Section 4.4 concludes the discussions in this chapter.

4.1 Basic protocol

The entanglement generation utilizes the same schematic setup as we proposed in Fig. 2.1(a). We focus on a specific device composed of a single charged quantum dot coupled to a single-sided optical cavity that supports one mode with well-defined polarization. We assume an external magnetic field is applied in the Voigt geometry. In this configuration, the energy level structure of the quantum dot is shown in Fig. 1.2(b). We assume the cavity field is polarized along the V direction, which can only couple to the quantum dot vertical transitions σ_1 and σ_4. This condition can be attained by aligning the direction of the magnetic field with the cavity polarization. We also assume that the transition σ_1 is resonant with the cavity mode, while transition σ_4 is detuned.

We define the qubit basis of the photon as $|D\rangle = (|H\rangle + |V\rangle)/\sqrt{2}$ and $|A\rangle = (|H\rangle - |V\rangle)/\sqrt{2}$. To create entanglement between the quantum dot and photon, the quantum dot qubit is first prepared to the superposition state $(|\uparrow\rangle + |\downarrow\rangle)/\sqrt{2}$, which can be achieved by optical pumping followed by all-optical coherent control, as we demonstrated in Chapter 3. The photonic qubit is prepared in the $|D\rangle$ state and reflects off the cavity mode. Upon reflection from the cavity, the photon polarization will be transformed to $|D\rangle \rightarrow (|H\rangle + r_{\uparrow(\downarrow)}|V\rangle)/\sqrt{2}$, where $r_{\uparrow(\downarrow)} = (C_{\uparrow(\downarrow)} - 1)/(C_{\uparrow(\downarrow)} +$

1) is the cavity reflection coefficient, and $C_{\uparrow(\downarrow)}$ is the spin-dependent cooperativity given by (see detailed derivations in Section 2.1)

$$C_{\uparrow} = 2g^2/\kappa\gamma \tag{4.1}$$

$$C_{\downarrow} = 2g^2/\kappa(\gamma - i\Delta_z) \tag{4.2}$$

The parameter Δ_z is the frequency difference between the two vertical transitions, given by $\Delta_z = \Delta_e + \Delta_h$, where $\Delta_e = g_e\mu_B B/\hbar$ and $\Delta_h = g_h\mu_B B/\hbar$ are the Zeeman splitting for the ground states and trion states respectively, g_e and g_h are the Lande g-factor for the electron and hole, respectively, B is the magnitude of the applied magnetic field, and μ_B is the Bohr magneton. The remaining parameters g, γ and κ are the quantum dot - cavity coupling strength, the trion state dipole decay rate, and the cavity photon decay rate respectively. In the above equations, we have assumed that the incident photon is monochromatic and resonant with the cavity frequency, and the cavity is perfect single sided ($\alpha = 1$).

In the limit where $\Delta_z \gg 2g^2/\kappa$ (large detuning) and $C_{\uparrow} \gg 1$ (high cooperativity), we have $r_{\uparrow} = 1$ and $r_{\downarrow} = -1$. Therefore the photonic qubit is unchanged if the quantum dot is in spin-up state ($|\uparrow\rangle|D\rangle \rightarrow |\uparrow\rangle|D\rangle$), but flipped if the quantum dot is in spin down state ($|\downarrow\rangle|D\rangle \rightarrow |\downarrow\rangle|A\rangle$). Because the spin qubit is initially prepared to an equal superposition of spin-up and spin-down states, the reflection of the photon will generate the spin-photon entangled state $(|\uparrow\rangle|D\rangle + |\downarrow\rangle|A\rangle)/\sqrt{2}$.

4.2 General expression for entanglement fidelity

The protocol described in Section 4.1 generates an ideal entangled state in the limit where the photon is monochromatic, the resonant cooperativity is large, and the detuning between the vertical transitions is large. In order to investigate the performance of the protocol under more realistic conditions, we derive a general expression for the fidelity of the generated entangled state. We define the entanglement fidelity as $F = |\langle\psi_d|\psi_f\rangle|^2$, where $|\psi_d\rangle$ is the desired final state, and $|\psi_f\rangle$ is the generated final state.

To attain an expression for $|\psi_d\rangle$ and $|\psi_f\rangle$, we focus on the case where the entire system contains only a single excitation, and express the general state of the system in the basis $|\alpha, \beta\rangle$ where $\alpha \in \{\uparrow, \downarrow, \Uparrow, \Downarrow\}$ is the state of the quantum dot, and $\beta \in \{C, V_\delta, H_\delta, 0\}$ describes the state of the photon. In the expression for the photonic component, C denotes a photon in the cavity, V_δ and H_δ indicates that the photon is in the external mode that drives the cavity and has a polarization V or H with a detuning δ, and 0 indicates that all photonic modes are in vacuum (i.e. the excitation is contained in the quantum dot). The general state of the system at time t is

$$\begin{aligned} |\psi(t)\rangle = {} & c_\uparrow(t)|\uparrow, C\rangle + c_\downarrow(t)|\downarrow, C\rangle + c_\Uparrow(t)|\Uparrow, 0\rangle + c_\Downarrow(t)|\Downarrow, 0\rangle \\ & + \int_{-\infty}^{\infty} \left[p_\uparrow(\delta, t)|\uparrow, V_\delta\rangle + p_\downarrow(\delta, t)|\downarrow, V_\delta\rangle\right] d\delta \\ & + \int_{-\infty}^{\infty} \left[q_\uparrow(\delta, t)|\uparrow, H_\delta\rangle + q_\downarrow(\delta, t)|\downarrow, H_\delta\rangle\right] d\delta \end{aligned} \tag{4.3}$$

where the coefficient c_α represents the probability amplitude when the excitation is contained in the cavity, either as a photon or as a quantum dot excitation. The

amplitudes $p_{\uparrow(\downarrow)}(\delta, t)$ and $q_{\uparrow(\downarrow)}(\delta, t)$ account for the cases where the photon is in the V and H polarized external cavity mode that has a detuning δ, respectively.

We first obtain an expression for the initial state of the system $|\psi_i\rangle$, from which we can calculate both $|\psi_d\rangle$ and $|\psi_f\rangle$. Initially, the single excitation is contained in the external photonic mode. Therefore we have $c_\alpha(t_i) = 0$, where t_i is the time that the photon arrives at the cavity. In addition, since the quantum dot is initially prepared in an equal superposition state between $|\uparrow\rangle$ and $|\downarrow\rangle$, and the photon is initially prepared in the polarization state $(|H\rangle + |V\rangle)/\sqrt{2}$, the coefficients for the initial state satisfies $p_\uparrow(\delta, t_i) = p_\downarrow(\delta, t_i) = q_\uparrow(\delta, t_i) = q_\downarrow(\delta, t_i)$. Therefore we can write the initial state

$$|\psi_i\rangle = \int_{-\infty}^{\infty} \frac{u(\delta)}{2}(|\uparrow, V_\delta\rangle + |\downarrow, V_\delta\rangle + |\uparrow, H_\delta\rangle + |\downarrow, H_\delta\rangle)d\delta, \tag{4.4}$$

where we set $u(\delta) = 2p_{\uparrow(\downarrow)}(\delta, t_i) = 2q_{\uparrow(\downarrow)}(\delta, t_i)$. The additional factor of 2 is selected to ensure that $u(\delta)$ satisfies the normalization condition $\int_{-\infty}^{\infty} u^*(\delta)u(\delta)d\delta = 1$.

The final state of the system takes similar expression, given by

$$\begin{aligned} |\psi_f\rangle = & \int_{-\infty}^{\infty} \left[p_\uparrow(\delta, t_f)|\uparrow, V_\delta\rangle + p_\downarrow(\delta, t_f)|\downarrow, V_\delta\rangle\right] d\delta \\ & + \int_{-\infty}^{\infty} \frac{u(\delta)}{2}(|\uparrow, H_\delta\rangle + |\downarrow, H_\delta\rangle)d\delta \end{aligned} \tag{4.5}$$

Note that as the cavity is polarized in V direction, the H polarization component of the external photon does not enter the cavity and gets directly reflected. Therefore the coefficients for the H polarized photon remain the same as the initial state of the system. We can also obtain the desired final state $|\psi_d\rangle$ by applying the ideal transform relation $|\uparrow\rangle|D\rangle \rightarrow |\uparrow\rangle|D\rangle$ and $|\downarrow\rangle|D\rangle \rightarrow |\downarrow\rangle|A\rangle$ to the initial state of the

system $|\psi_i\rangle$, given by

$$|\psi_d\rangle = \int_{-\infty}^{\infty} \frac{u(\delta)}{2}(|\uparrow, V_\delta\rangle - |\downarrow, V_\delta\rangle + |\uparrow, H_\delta\rangle + |\downarrow, H_\delta\rangle)d\delta \tag{4.6}$$

Using the expressions of $|\psi_d\rangle$ and $|\psi_f\rangle$, we obtain the expression for the fidelity, given by

$$F = \left|\frac{1}{2} + \frac{1}{2}\int_{-\infty}^{\infty} u^*(\delta)\big[p_\uparrow(\delta, t_f) - p_\downarrow(\delta, t_f)\big]d\delta\right|^2 \tag{4.7}$$

Sometimes it is more convenient to express the fidelity in the time domain, given by

$$F = \left|\frac{1}{2} + \frac{1}{2}\int_{-\infty}^{\infty} f_{in}^*(t)\big[f_{out}^{\uparrow}(t) - f_{out}^{\downarrow}(t)\big]dt\right|^2, \tag{4.8}$$

where the time varying function $f_{in}(t)$ represents the amplitude of the input photon pulse, given by

$$f_{in}(t) = \int_{-\infty}^{\infty} u(\delta)e^{-i\delta(t-t_i)}d\delta, \tag{4.9}$$

and we define the cavity output field amplitudes $f_{out}^{\uparrow}(t)$ and $f_{out}^{\downarrow}(t)$ as

$$f_{out}^{\uparrow(\downarrow)}(t) = \int_{-\infty}^{\infty} p_{\uparrow(\downarrow)}(\delta, t_f)e^{-i\delta(t-t_f)}d\delta, \tag{4.10}$$

where t_f is taken to be sufficiently large such that the photon has left the cavity. The spin-dependent time output fields are related to the input field by the cavity input-output relations

$$f_{out}^{\uparrow(\downarrow)}(t) = f_{in}(t)/2 - \sqrt{\kappa}c_{\uparrow(\downarrow)}(t) \tag{4.11}$$

In order to calculate the fidelity, we need to obtain an expression for $c_{\uparrow(\downarrow)}(t)$. We begin with the expression for the Hamiltonian of a coupled quantum dot - cavity system where the quantum dot exhibits the energy level structure shown in

Fig. 1.2(b). We define the center frequency of the incident photon as ω, and express the Hamiltonian in a reference frame rotated with respect to ω. We express the Hamiltonian as where $\hat{\mathbf{H}} = \hat{\mathbf{H}}_\mathbf{0} + \hat{\mathbf{H}}_\mathbf{int} + \hat{\mathbf{H}}_\mathbf{d}$, where

$$\begin{aligned}
\hat{\mathbf{H}}_\mathbf{0} &= \hbar\Delta_c \hat{\mathbf{a}}^\dagger \hat{\mathbf{a}} + \hbar\Delta_x \hat{\sigma}_1^\dagger \hat{\sigma}_1 + \hbar(\Delta_x - \Delta_z)\hat{\sigma}_4^\dagger \hat{\sigma}_4 \\
&\quad + \int_{-\infty}^{\infty} \hbar\delta \big[\hat{\mathbf{b}}_\mathbf{V}^\dagger(\delta)\hat{\mathbf{b}}_\mathbf{V}(\delta) + \hat{\mathbf{b}}_\mathbf{H}^\dagger(\delta)\hat{\mathbf{b}}_\mathbf{H}(\delta)\big] d\delta \qquad (4.12) \\
\hat{\mathbf{H}}_\mathbf{int} &= i\hbar g_V(\hat{\sigma}_1^\dagger + \hat{\sigma}_4^\dagger)\hat{\mathbf{a}} + i\hbar g_C(e^{i\Delta_e t}\hat{\sigma}_2^\dagger + e^{-i\Delta_e t}\hat{\sigma}_3^\dagger)\hat{\mathbf{a}} + \text{H.c.} \qquad (4.13) \\
\hat{\mathbf{H}}_\mathbf{d} &= \int_{-\infty}^{\infty} \hbar R \hat{\mathbf{b}}_\mathbf{V}^\dagger(\delta)\hat{\mathbf{a}} d\delta + \text{H.c.} \qquad (4.14)
\end{aligned}$$

In the above equations, $\hat{\sigma_1}$ - $\hat{\sigma_4}$ is the lowering operator for quantum dot transitions σ_1 to σ_4 respectively; $\hat{\mathbf{a}}$ is the photon annihilation operator for the cavity mode; $\hat{\mathbf{b}}_\mathbf{H}(\delta)$ and $\hat{\mathbf{b}}_\mathbf{V}(\delta)$ are the photon annihilation operators for the V and H polarized external cavity modes that drive the cavity and have a frequency of $\omega + \delta$. The parameters Δ_c and Δ_x are given by $\Delta_c = \omega_c - \omega$ and $\Delta_x = \omega_x - \omega$, where ω_c is the cavity resonance frequency, and ω_x is the frequency of the dot transition σ_1. The parameters $g_V(g_C)$ is the coupling strength between the cavity and the quantum dot vertical (cross) transitions; and R is the coupling strength between the cavity and the V-polarized external cavity modes. We have made the Markov approximation where R is independent of frequency over a wide bandwidth centered around $\delta = 0$. We have included the coupling term between the cross transitions of the quantum dot and the cavity. These coupling terms account for the possible misalignment of the external magnetic field with the cavity polarization axis. For a perfect alignment we have $g_C = 0$.

The state of the system evolves according to Schrodingers equation $i\hbar\frac{\partial}{\partial t}|\psi(t)\rangle =$

$\hat{\mathbf{H}}|\psi(t)\rangle$. Using the definition of $\psi(t)$ in Eq. 4.3 and the Hamiltonian given in Eq. 4.12 - Eq. 4.14, we obtain the following differential equation for the probability amplitudes of the internal states of the quantum dot - cavity system:

$$\frac{d}{dt}c_{\uparrow}(t) = -(i\Delta_c + \kappa/2)c_{\uparrow}(t) - g_V^* c_{\Uparrow}(t) - g_C^* e^{-i\Delta_e t}c_{\Downarrow}(t) + \sqrt{\kappa}\frac{f_{in}(t)}{2} \quad (4.15)$$

$$\frac{d}{dt}c_{\downarrow}(t) = -(i\Delta_c + \kappa/2)c_{\downarrow}(t) - g_C^* e^{i\Delta_e t}c_{\Uparrow}(t) - g_V^* c_{\Downarrow}(t) + \sqrt{\kappa}\frac{f_{in}(t)}{2} \quad (4.16)$$

$$\frac{d}{dt}c_{\Uparrow}(t) = -(i\Delta_x + \gamma)c_{\Uparrow}(t) + g_V c_{\uparrow}(t) + g_C e^{-i\Delta_e t}c_{\downarrow}(t) \quad (4.17)$$

$$\frac{d}{dt}c_{\Downarrow}(t) = -\big[i(\Delta_x - \Delta_z) + \gamma\big]c_{\Downarrow}(t) + g_C e^{i\Delta_e t}c_{\uparrow}(t) + g_V c_{\downarrow}(t) \quad (4.18)$$

We have added the decay term γ to the exciton probability amplitudes $c_{\Uparrow}(t)$ and $c_{\Downarrow}(t)$ to account for spontaneous emission of the quantum dot trion states. The parameter $\kappa = 2\pi R^2$ accounts for the decay rate of the cavity photon to the V polarized external cavity modes. By solving Eq. 4.15 - 4.18, we are able to obtain $c_{\uparrow(\downarrow)}(t)$, from which we can calculate the system fidelity based on Eq. 4.8 and Eq. 4.11.

4.3 Analysis of entanglement fidelity

We first consider the fidelity in the quasi-monochromatic limit. In this limit, the incident photon amplitude $f_{in}(t)$ varies sufficiently slowly so that we can analyze the process in the adiabatic limit. We attain an analytical solution for $f_{out}^{\uparrow(\downarrow)}(t)$ by adiabatically eliminating Eq. 4.15 - 4.18. We assume for now that the magnetic field is aligned with the cavity mode so that $g_C = 0$ (we will re-visit this assumption),

which gives

$$f_{out}^{\uparrow}(t) = \frac{1}{2}\left(1 - \frac{2}{1 + 2\left|g_V\right|^2/\kappa\gamma}\right) \tag{4.19}$$

$$f_{out}^{\downarrow}(t) = \frac{1}{2}\left(1 - \frac{2}{1 + 2\left|g_V\right|^2/\kappa(\gamma - i\Delta_z)}\right) \tag{4.20}$$

We can therefore calculate the entanglement fidelity, given by

$$F = \left|\frac{1}{2} + \frac{1}{4}\left(\frac{C_\uparrow - 1}{C_\uparrow + 1} - \frac{C_\downarrow - 1}{C_\downarrow + 1}\right)\right|^2, \tag{4.21}$$

where $C_\uparrow$ and $C_\downarrow$ have been previously defined in Eq. 4.1 and Eq. 4.2 respectively. We obtain an ideal fidelity of $F = 1$ when $|C_\uparrow| \gg 1$ and $|C_\downarrow| \ll 1$, consistent with the ideal case described in Section 4.1. However, $C_\uparrow$ and $C_\downarrow$ are not independent variables, they are relate by $C_\downarrow = C_\uparrow/(1 - i\Delta_z/\gamma)$. Thus, for a finite value of Δ_z and γ, the two conditions $|C_\uparrow| \gg 1$ and $|C_\downarrow| \ll 1$ cannot be achieved simultaneously.

Figure 4.1(a) shows the fidelity as a function of the cooperativity $C_\uparrow$ for several values of the magnetic field magnitude B. We assume the Lande g-factors for the electron and hole are given by $g_e = 0.43$ and $g_h = 0.21$, respectively [101], and we set $\gamma/2\pi = 0.15$ GHz [83]. The initial increase in $C_\uparrow$ results in a higher fidelity because the condition $|C_\uparrow| \gg 1$ becomes better satisfied. At even larger cooperativity the fidelity achieves a maximum and begins to decline because the condition $|C_\downarrow| \ll 1$ is no longer well-satisfied. Figure 4.1(b) plots the optimal fidelity as a function of the magnetic field magnitude B. At $B = 9$ T, the optimal fidelity can be as high as 0.974. Interestingly, in contrast to previously proposed protocol [28–31], this protocol achieves higher fidelities with increasing magnetic field.

We next investigate the entanglement fidelity for an input field that is not quasi-monochromatic. We excite the system with a Gaussian input pulse given by

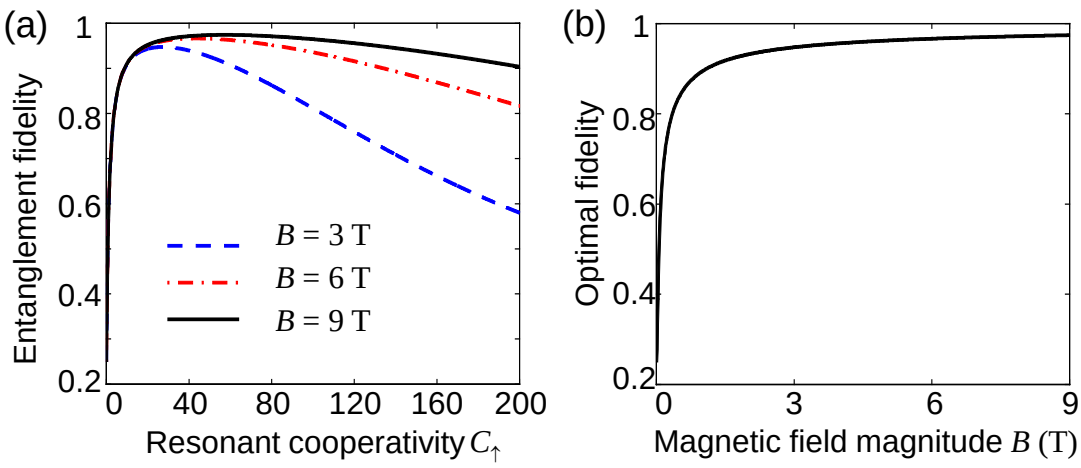

Figure 4.1: Entanglement fidelity as a function of cooperativity and magnetic field magnitude. (a) Entanglement fidelity as a function of the cooperativity $C_\uparrow$ for several different values of the magnetic field magnitude B. (b) Optimal fidelity as a function of the magnetic field magnitude B.

$f_{in}(t) = \left[\frac{1}{\sqrt{2\pi}\tau}\exp(-t^2/\tau^2)\right]^{1/2}$. The parameter τ characterizes the pulse duration, and represents the half-width of the pulse at $1/e$ of the maximum. We set $g_V/2\pi =$ 11 GHz, $\kappa/2\pi = 25$ GHz, which are achievable in a quantum dot - cavity quantum electrodynamics system [83], and $\gamma/2\pi = 0.15$ GHz [83]. These parameters achieve the optimal cooperativity in the monochromatic limit for $B = 9$ T.

We numerically solve Eq. 4.15 - Eq. 4.18 and calculate the entanglement fidelity using Eq. 4.8. Figure 4.2 plots the fidelity as a function of the photon pulse width τ. The dashed line in the figure indicates the fidelity in the quasi-monochromatic limit. The fidelity makes a rapid transition from $F = 0.974$ to $F = 0.25$ at a critical pulse width of $\tau \simeq 100$ ps. This degradation in fidelity can be understood most easily using a frequency domain picture. When the quantum dot is in the

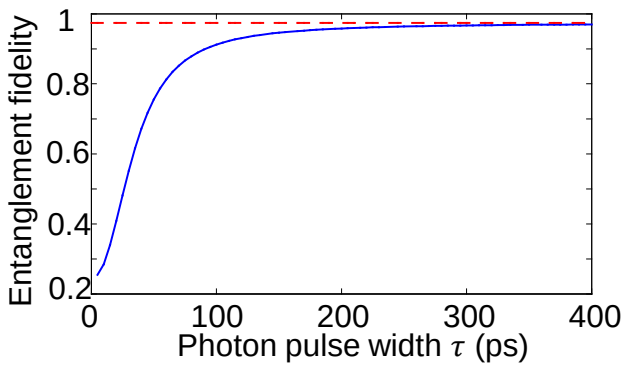

Figure 4.2: Entanglement fidelity as a function of the photon pulse width (blue solid line). The red dashed line indicates the fidelity in the quasi-monochromatic limit.

spin-up state, the cavity reflection spectrum will be strongly modified only within a spectral bandwidth given by the vacuum Rabi splitting in the strong coupling regime, and the modified quantum dot lifetime in the weak coupling regime [14]. As the pulse duration of the input photon continues to be reduced, its spectrum no longer fits within this spectral window, leading to a degradation of the fidelity of the generated state. We can achieve near unity fidelity with pulse width on the order of 200 ps, which is much shorter than the typical decoherence time of the quantum dot spin [20, 21].

Finally, we analyze the entanglement fidelity when the external magnetic field is not perfectly aligned to the cavity. In this case both the vertical and the cross transitions of the quantum dot can couple with the cavity. The coupling strength is given by $g_V = g\cos\theta$ and $g_C = ig\sin\theta$, where θ is the angle between the magnetic field and the cavity axis. The factor i indicates the $\pi/2$ phase difference between the dipole moments of the vertical and cross transitions of the quantum dot.

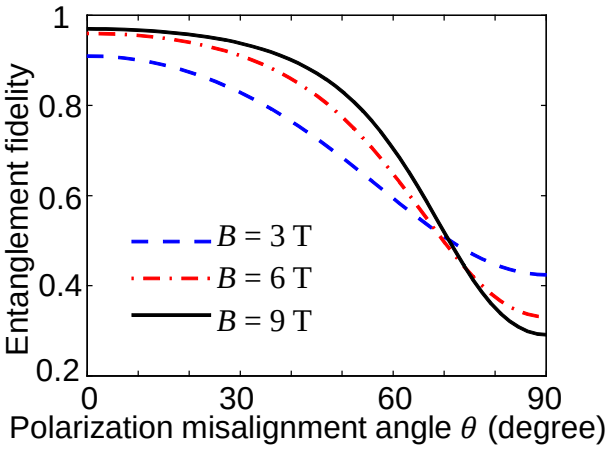

Figure 4.3: Entanglement fidelity as a function of the polarization misalignment angle θ for several different values of the magnetic field magnitude B.

The coupling between the cavity and the quantum dot cross transitions provides a channel for spin flipping when the photon is interacting with cavity [102], which is undesired in our protocol and degrades the entanglement fidelity. Figure 4.3 shows the fidelity as a function of θ for several values of the magnetic field magnitude. We assume a Gaussian input pulse with pulse width of $\tau = 400$ ps and numerically calculate the fidelity using Eq. 4.15 - Eq. 4.18 and Eq. 4.8. We set $g/2\pi = 11$ GHz (equal to g_V in the previous calculation), while all other parameters are identical to those used in the calculations for Fig. 4.2. The results show that our entanglement protocol is robust to misalignment of the magnetic field, and can tolerate angular mismatches of tens of degrees.

4.4 Discussions

We have proposed and analyzed a protocol for deterministic generation of entanglement between a quantum dot spin and a photon. The protocol does not require temporal post-selection, and could therefore provide significantly improved efficiency. In addition, the protocol is feasible to realize using currently achievable quantum dot - cavity quantum electrodynamics systems. These results could provide a promising approach for realization of solid states quantum networks and distributive quantum computations using semiconductor nanophotonic devices.

Chapter 5: Cavity enhanced optical spin readout

The ability to projectively measure the state of a qubit with high accuracy is crucial for nearly all quantum information processing applications [103]. In the majority of applications, these qubit measurements must be performed in a single shot [64]. For example, quantum computing requires the ability to read out the states of all output qubits after the quantum algorithm completes [104–106], and quantum cryptography requires readout of all transmitted qubits [107]. Single-shot qubit readout also plays an important role in quantum error corrections [108], quantum teleportation [109], and experimental measurements of quantum non-locality [110].

Resonance fluorescence spectroscopy is currently one of the most effective ways to perform optical single-shot readout. However, this approach requires a good cycling transition where an excited state optically couples to only one of the qubit basis states. The cycling transition yields a large number of resonance fluorescence photons for one basis state, enabling strong optical signal even with poor detection efficiency, while yielding very few photons for the other state. Previous studies have demonstrated single-shot readout with resonance fluorescence in a number of qubit systems, including cold atoms [111], trapped ions [112,113], nitrogen vacancy

centers [114, 115] and quantum dot molecules [116]. However, many qubit systems, especially solid-state qubit systems, do not possess a good cycling transition due to non-radiative decay mechanisms or selection rules. These qubit systems include quantum dot spins [63], fluorine impurities in CdTe [117], and silicon vacancy centers [118, 119].

Cavity quantum electrodynamics provides an alternative approach to optically detect the qubit. In contrast to resonance fluorescence, this approach exploits strong light-matter interactions where the qubit state modulates the reflectance or transmittance of a cavity. Several experiments have utilized the reflection and transmission of a cavity to measure the hyperfine state of a single atom [120, 121]. A number of theory works have proposed cavity enhanced solid-state qubit readout [16, 122–124]. However, experimental demonstration of this approach in a solid-state qubit system remains a grand challenge.

In this chapter, we propose a protocol for single-shot optical readout of a qubit that lacks a good cycling transition based on a cavity QED system, and demonstrate it experimentally using a specific system composed of a strongly coupled charged quantum dot and a photonic crystal cavity. This chapter is organized as follows. Section 5.1 describes the protocol for using a cavity QED system to perform spin readout. Section 5.2 provides theoretical analysis of the spin readout fidelity based on our protocol, and demonstrates the feasibility to achieve single-shot readout for a quantum dot spin in the Voigt configuration. In Section 5.3, we experimentally demonstrate cavity enhanced optical spin readout, using a specific system composed of a charged quantum dot in the Faraday configuration that is strongly coupled to

a photonic crystal cavity. Section 5.4 concludes the discussions in this chapter.

5.1 Basic protocol

The optical spin readout utilizes the same schematic setup as shown in Fig. 2.1, which is consisted of a generic qubit system coupled to an optical cavity. Similar as the analysis in Section 2.2, we assume that the cavity is single-sided and supports only one mode with well-defined polarization in the y direction. We also assume that the qubit system has a λ-type energy structure as shown in Fig. 2.1(b), with two ground states that form a stable spin qubit, denoted as $|\uparrow\rangle$ and $|\downarrow\rangle$, and one excited state $|e\rangle$ that gives rise to spin-dependent optical transitions $\mu_\uparrow$ and $\mu_\downarrow$ respectively. When exciting one of the two transitions, suppose $\mu_\uparrow$, the emitter will emit no photons when it is in the spin-down state, but emit N photons when it is in the spin-up state. In the ideal case where the linewidth of both transitions is radiatively limited, N is given by the branching ratio $N = \gamma_\uparrow/\gamma_\downarrow$, where $\gamma_\uparrow$ and $\gamma_\uparrow$ are the spontaneous emission rates for transitions $\mu_\uparrow$ and $\mu_\downarrow$ respectively. A qubit system has a good cycling transition if $N \gg 1$. In contrast to resonance fluorescence techniques that require a good cycling transition, here we are primarily interested in the situation where the two optical transitions have similar dipole strength so that the qubit system does not possess a good cycling transition.

To perform optical readout, we consider the case where optical transition $\mu_\uparrow$ is resonant with the cavity while transition $\mu_\downarrow$ is decoupled, either by a large detuning or by selection rules if transition $\mu_\downarrow$ emits a photon with a different polarization than

the cavity mode. In this configuration the coupling between the atom and cavity depends on the qubit state. The cavity thus exhibits spin-dependent reflection coefficients as shown in Section 2.1, enabling qubit readout by optically probing the cavity.

We start the protocol by resonantly probing the cavity reflectivity using a pulsed laser of a duration T. We define the incident photon flux as n_{in} (in units of photons per second). We assume $n_{in} \ll 1/\tau$ where τ is the modified lifetime of the excited state. Thus, the system operates in the weak excitation regime. Suppose the incident field is polarized in the diagonal direction $\vec{d}$ ($\vec{d} = (\vec{x}+\vec{y})/\sqrt{2}$). In the absence of spin flip, the average number of photons collected in the anti-diagonal polarization basis $\vec{a}$ ($\vec{a} = (\vec{x} - \vec{y})/\sqrt{2}$) is given by $N_{\uparrow}(T) = \eta T n_{in}/(1+C)^2$ and $N_{\downarrow} = \eta T n_{in}$ respectively [14, 88, 89], where $N_{\uparrow}(T)$ and $N_{\downarrow}(T)$ represents the average number of collected photons when the qubit is in spin-up and spin-down state respectively, and η is photon overall collection efficiency that accounts for coupling efficiency of the optics, imperfect spatial mode matching between the incident photon and the cavity, and quantum efficiency of the detector, and C is the system cooperativity.

To determine the spin state, we compare the number of collected photons with a threshold photon number k. When the number of collected photons is less than k the measurement result reports a qubit state $|\uparrow\rangle$, otherwise it reports state $|\downarrow\rangle$. Note that the photons collected in both the diagonal and anti-diagonal polarization basis could in principle be used to measure the qubit. Our analysis will focus on the photons collected at the anti-diagonal polarization basis, and the results will apply for both cases.

We define the spin readout fidelity as $F = \max_k [q_\uparrow p_\uparrow(k) + q_\downarrow p_\downarrow(k)]$, where $q_\uparrow$ and $q_\downarrow$ is the probability that the spin occupies spin-up and spin-down state respectively, and $p_\uparrow(k)$ and $p_\downarrow(k)$ is the probability of getting a correct result using threshold photon number k when the spin is initially in the spin-up and spin-down state respectively. If the dominant noise for the collected photon number is shot noise (which is a valid assumption in the weak excitation regime provided that the detector dead time is much short compared to the photon arrival rate), the expression of the fidelity is given by

$$F(T) = \frac{1}{2} + \frac{1}{2}\sum_{j=0}^{M} \frac{1}{j!}\left([N_\uparrow(T)]^j e^{-N_\uparrow(T)} - [N_\downarrow(T)]^j e^{-N_\downarrow(T)}\right) \tag{5.1}$$

where $M = \left\lfloor \frac{N_\downarrow(T) - N_\uparrow(T)}{\ln[N_\downarrow(T)] - \ln[N_\uparrow(T)]} \right\rfloor$ is the threshold photon number that gives the optimal fidelity, and $\lfloor x \rfloor$ indicates the largest integer that is not greater than x. In this derivation we have assumed $q_\uparrow = q_\downarrow = 0.5$, since in general one has no a-priori knowledge about the occupation probability of the two spin states.

Figure 5.1 shows the spin readout fidelity as a function of T for several different values of the cooperativity. The fidelity grows monotonically with T because we collect more photons. We are able to achieve near unity fidelity as long as the probe pulse duration is long enough, even for a very small cooperativity. The ripples in the plot are because the optimal threshold photon number can only increase by a discrete step of 1.

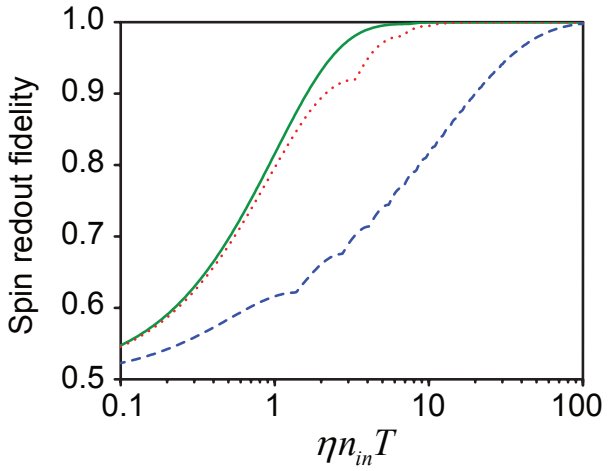

Figure 5.1: Spin readout fidelity as a function of probe pulse duration for several different values of cooperativity. Blue dashed line, C = 0.4; red dotted line, C = 4; green solid line, C = 40.

5.2 Theoretical analysis of spin readout fidelity

5.2.1 Derivation of fidelity in the presence of spin flip

In the previous section we showed that the fidelity of the spin readout operation monotonically increases with the probe pulse duration and can eventually approach unity. However, the probe pulse duration is fundamentally limited by the laser induced spin flip which causes measurement errors. Thus, to accurately calculate the fidelity, we need a model that incorporates both cavity reflectivity modification and spin flip errors.

We still perform our calculation in the weak excitation regime. In this regime Eq. 5.1 remains valid, but we need to derive the expressions for $N_{\uparrow}(T)$ and $N_{\downarrow}(T)$ in the presence of spin flips, which no longer holds a simple linear relationship with

T. We can calculate $N_\uparrow$ and $N_\downarrow$ by integrating the photon output flux of the cavity over the time duration T, given by

$$N_{\uparrow(\downarrow)}(T) = \eta \int_0^T \left| Tr\left(\sqrt{\kappa}\hat{\mathbf{a}}\rho_{\uparrow(\downarrow)}(t)\right)\right|^2 dt \tag{5.2}$$

where $\hat{\mathbf{a}}$ is the photon annihilation operator for the cavity mode, $\rho_{\uparrow(\downarrow)}(t)$ is the density matrix of the system at time t when the qubit is initialized in the spin-up and spin-down state at $t = 0$ respectively.

To calculate $\rho_{\uparrow(\downarrow)}(t)$, we numerically solve the system dynamics using the master equation given by $d\rho/dt = -(i/\hbar)[\hat{\mathbf{H}}, \rho] + \hat{\mathbf{L}}\rho$, where $\hat{\mathbf{H}}$ is the system Hamiltonian that accounts for all unitary processes, and $\hat{\mathbf{L}}$ is the Liouvillian superoperator that accounts for all non-unitary Markovian processes. We write the system Hamiltonian in a reference frame with respect to the frequency of the incident field ω, given by $\hat{\mathbf{H}} = \hat{\mathbf{H}}_\mathbf{0} + \hat{\mathbf{H}}_\mathbf{int} + \hat{\mathbf{H}}_\mathbf{d}$, where

$$\hat{\mathbf{H}}_\mathbf{0} = \hbar(\omega_c - \omega)\hat{\mathbf{a}}^\dagger\hat{\mathbf{a}} + \hbar(\omega_x - \omega)|e\rangle\langle e| \tag{5.3}$$

$$\hat{\mathbf{H}}_\mathbf{int} = ig\hbar(\hat{\mathbf{a}}|e\rangle\langle\uparrow| - \hat{\mathbf{a}}^\dagger|\uparrow\rangle\langle e|) \tag{5.4}$$

$$\hat{\mathbf{H}}_\mathbf{d} = \hbar\sqrt{\kappa}\epsilon(\hat{\mathbf{a}} + \hat{\mathbf{a}}^\dagger) \tag{5.5}$$

In Eq. 5.3 - Eq. 5.5, ω_c is the frequency of the cavity mode, and ω_x is the frequency of the transition $\mu_\uparrow$.

The Liouvillian superoperator $\hat{\mathbf{L}}$ accounts for the decay of the cavity field and spontaneous emission of each optical transition. This operator is given by

$$\hat{\mathbf{L}} = \kappa D(\hat{\mathbf{a}}) + \gamma_1 D(|\uparrow\rangle\langle e|) + \gamma_2 D(|\downarrow\rangle\langle e|) \tag{5.6}$$

where $D(\hat{\mathbf{O}}) = \hat{\mathbf{O}}\rho\hat{\mathbf{O}}^\dagger - \frac{1}{2}\hat{\mathbf{O}}^\dagger\hat{\mathbf{O}}\rho - \frac{1}{2}\rho\hat{\mathbf{O}}^\dagger\hat{\mathbf{O}}$ is the general Linblad operator form for

the collapse operator $\hat{\mathbf{O}}$. The transition linewidth can also be broadened due to trion dephasing and spectral diffusion, which we will revisit in Section 5.2.3.

5.2.2 Analysis of fidelity for a quantum dot based cavity QED system

In this section, we perform numerical calculations on a specific case of a charged quantum dot coupled to a photonic crystal defect cavity. Both multi-shot [71, 72] and single-shot [73] spin readout has been demonstrated for a charged quantum dot with a magnetic field applied in the Faraday configuration, by using resonance fluorescence spectroscopy. But the highest spin readout fidelity reported so far is only $\sim 84\%$, limited by the imperfect cycling transition caused by the non-radiative decay mechanism for the optical forbidden transitions. In addition, it is more desired to realize single-shot spin readout in the Voigt configuration because this geometry is the prerequisite for all-optical coherent spin manipulation [21–26]. The selection rules in the Voigt configuration does not support a cycling transition, eliminating the possibility for single-shot readout using typical fluorescence light detection technique.

In the Voigt configuration, the energy level structure of the quantum dot is shown in Fig. 1.2(b). Similarly as the entanglement protocol described in Section 4.1, we assume that the cavity field is polarized along the V direction, which can only couple to the quantum dot vertical transitions σ_1 and σ_4. We consider the case where transition σ_1 is resonant with the cavity mode and the probe laser, whereas transition σ_4 is detuned by Δ_z. In the limit where $\Delta_z \gg 2g^2/\kappa$, we could effectively

ignore the coupling between transition σ_4 and the cavity, and simplify the qubit system to the model depicted in Fig. 1.2(b). We will revisit this assumption in the later part of this section. We set the cavity parameters to $g/2\pi = 20$ GHz and $\kappa/2\pi = 6$ GHz [125]. For the quantum dot, we assume the spontaneous emission rate is 0.1 GHz for both optical transitions ($\gamma_1/2\pi = \gamma_2/2\pi = 0.1$ GHz) [57]. We set the incident photon field amplitude to $\epsilon = \sqrt{0.01 \times 2g^2/\kappa}$, which corresponds to an average incident photon number of 0.01 per modified lifetime of transition σ_1, to ensure that we are operating in the linear weak excitation regime.

The blue dashed line shown in Fig. 5.2(a) shows the fidelity as a function of laser pulse duration T for a photon collection efficiency of $\eta = 1\%$. The fidelity initially increases with T because we collect more photons, similar as the results shown in Fig. 5.1. At even larger T the fidelity achieves a maximum and begins to decline because the probing laser induces a spin-flip. We define the optimal fidelity as $F_{opt} = \max_T[F(T)]$, which achieves 0.995 with a time window of $T = 153$ ns.

We next investigate how a finite value of Δ_z affects the spin readout operation. In this case, we have to take into account the coupling between transition σ_4 and the cavity by using the four-level model (Fig. 1.2(b)) instead of the three-level model (Fig. 2.1(b)). We follow the same procedure described in Section 5.2.1 to calculate the fidelity, with slight modifications of the system Hamiltonian and Liouvillian superoperator. We still write the system Hamiltonian as $\hat{\mathbf{H}} = \hat{\mathbf{H}}_\mathbf{0} + \hat{\mathbf{H}}_\mathbf{int} + \hat{\mathbf{H}}_\mathbf{d}$, but

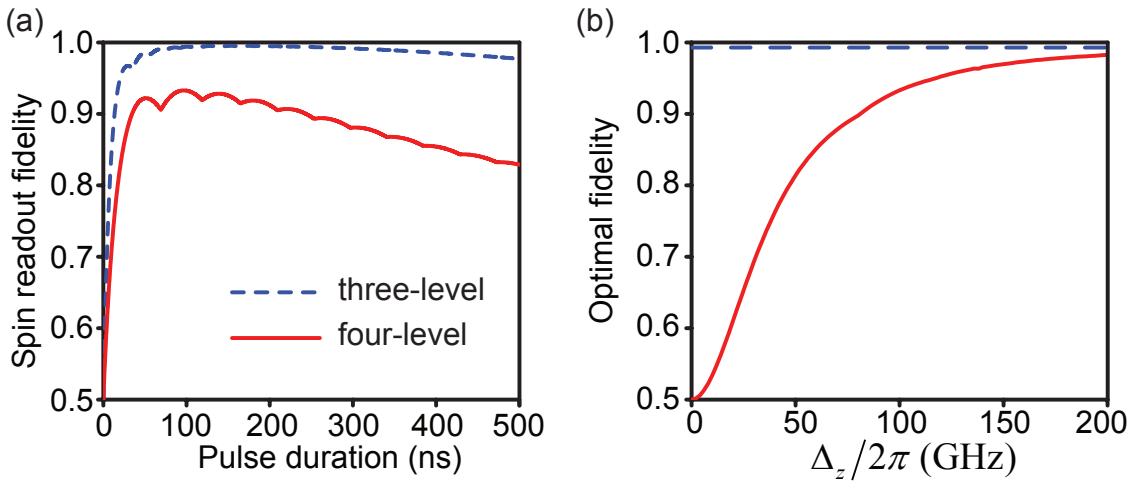

Figure 5.2: Spin readout fidelity in the presence of spin flips and finite Zeeman splitting. (a) Spin readout fidelity as a function of probe pulse duration calculated using the three-level model (blue dashed line) and the four-level model (red solid line). (b) Red solid line, optimal fidelity as a function of Δ_z. Blue dashed line, optimal fidelity calculated using a three-level model.

we modify $\hat{\mathbf{H}}_\mathbf{0}$ and $\hat{\mathbf{H}}_\mathbf{int}$ to

$$\hat{\mathbf{H}}_\mathbf{0} = \hbar(\omega_c - \omega)\hat{\mathbf{a}}^\dagger\hat{\mathbf{a}} + \hbar(\omega_x - \omega){\hat{\sigma_1}}^\dagger\hat{\sigma_1} + \hbar(\omega_x - \Delta_z - \omega){\hat{\sigma_4}}^\dagger\hat{\sigma_4} \tag{5.7}$$

$$\hat{\mathbf{H}}_\mathbf{int} = ig\hbar(\hat{\mathbf{a}}{\hat{\sigma_1}}^\dagger - \hat{\mathbf{a}}^\dagger\hat{\sigma_1}) + ig\hbar(\hat{\mathbf{a}}{\hat{\sigma_4}}^\dagger - \hat{\mathbf{a}}^\dagger\hat{\sigma_4}) \tag{5.8}$$

We also modify the Liouvillian superoperator as

$$\hat{\mathbf{L}} = \kappa D(\hat{\mathbf{a}}) + \gamma_1 D(\hat{\sigma_1}) + \gamma_2 D(\hat{\sigma_2}) + \gamma_3 D(\hat{\sigma_3}) + \gamma_4 D(\hat{\sigma_4}) \tag{5.9}$$

where γ_1 - γ_4 are the spontaneous emission rates for transitions σ_1 - σ_4 respectively. We again assume the spontaneous emission rate is 0.1 GHz for all optical transitions.

The red solid line in Fig. 5.2(a) shows the spin readout fidelity as a function of laser pulse duration T, calculated using the four-level model. In the calculation we set $\Delta_z/2\pi = 100$ GHz, corresponding to a magnetic field of 9.4 T [83], and keep all

other parameters the same as the calculations for the blue dashed line. The fidelity calculated using the four-level model has a similar trend as a function of T, with an optimal fidelity of 0.933. This value is lower than the value calculated using the three-level model since the cavity now couples to both spin states.

We further calculate the optimal fidelity as a function of Δ_z, shown as the red solid line in Fig. 5.2(b). When Δ_z is small, the cavity couples almost equally to two spin states, leading to a low value of spin readout fidelity. The optimal fidelity monotonically increases with Δ_z and approaches the value calculated using the three-level model (blue dashed line), because the coupling between transition σ_4 and the cavity becomes negligible.

Finally, we analyze the optimal fidelity as a function of the overall photon collection efficiency η. Figure 5.3 shows F_{opt} as a function of η, where all other parameters are set to be the same as the red solid line shown in Fig. 5.2(a). The fidelity increases with the collection efficiency and eventually approaches 1. At collection efficiency of 2.5% the fidelity achieves a value of 0.99. This efficiency is achievable with multiple cavity structures including photonic crystals [126–129] and micro-pillars [130, 131], and is also within the range of single photon counters [132].

5.2.3 The effect of emitter dephasing and spectral diffusion

To this point, we have assumed a radiatively limited linewidth for the optical transition of the qubit. In a realistic situation, the transition can be homogenously broadened due to dephasing [58], and inhomogeneously broadened due to spectral

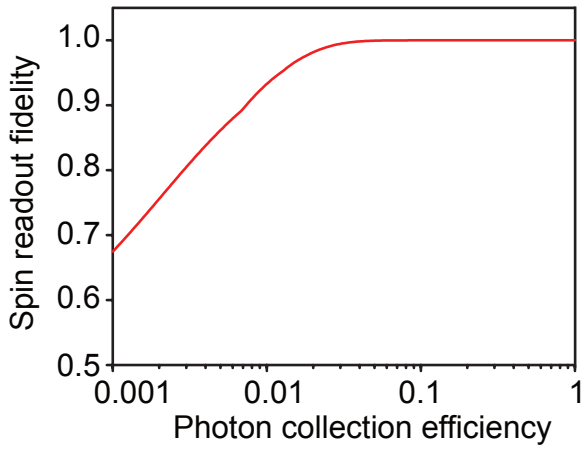

Figure 5.3: Spin readout fidelity as a function of photon overall collection efficiency η.

diffusion [38, 59–62], which might affect the spin readout fidelity. We still calculate the readout fidelity using the specific example of a quantum dot spin. To incorporate dephasing into our model, we introduce an additional term $\hat{\mathbf{L}}_\mathbf{d}$ in the Liouvillian superoperator given by

$$\hat{\mathbf{L}}_\mathbf{d} = 2\gamma_d D(\hat{\sigma_1}^\dagger \hat{\sigma_1}) + 2\gamma_d D(\hat{\sigma_4}^\dagger \hat{\sigma_4}) \tag{5.10}$$

The above expression assumes the same pure dephasing rate γ_d for both excited states $|\Uparrow\rangle$ and $|\Downarrow\rangle$. We calculate the system dynamics using the master equation $d\rho/dt = -(i/\hbar)[\hat{\mathbf{H}}, \rho] + (\hat{\mathbf{L}} + \hat{\mathbf{L}}_\mathbf{d})\rho$, where $\hat{\mathbf{L}}$ is given by Eq. 5.9.

The blue dashed line in Fig. 5.4 shows F_{opt} as a function of trion dephasing rate γ_d. We assume that $\eta = 2.5\%$, which achieves fidelity of 0.99 in the absence of linewidth broadening. We set all the other parameters to the same values as the ones used in the red solid line of Fig. 5.2(a). Increasing the trion dephasing rate

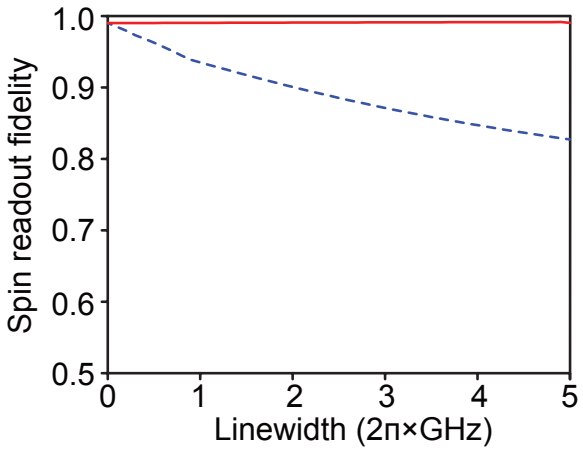

Figure 5.4: Spin readout fidelity as a function of quantum-dot homogeneously broadened linewidth γ_d (blue dashed line) and inhomogeneously broadened linewidth γ_I (red solid line).

reduces the cooperativity, which degrades the fidelity. For a typical trion dephasing rate $\gamma_d/2\pi = 1$ GHz, we are still able to achieve a fidelity as high as 0.93.

We next consider the effect of spectral diffusion, which could be caused by charge fluctuations [59, 60], thermal fluctuations [38], or nuclear spin noise [61, 62]. All of these mechanisms happen in a timescale that is slow compared to the modified trion state lifetime, but fast compared to the repetition time of a typical measurement. We can thus model it by setting ω_x as $\omega_x = \omega_x^{(0)} + \Delta\omega$, where $\omega_x^{(0)}$ is the average frequency of transition σ_1, and $\Delta\omega$ is a random variable corresponding to the frequency shift of transition σ_1 which may be different for each measurement shot. Here we only account for the spectral diffusion of transition σ_1 since the detuning between other transitions and the incident laser is much greater than their inhomogeneously broadened linewidth. We still assume the resonance condition where

$\omega = \omega_c = \omega_x^{(0)}$.

Following the same procedure as described in Section 5.2.2, we calculate the spin readout fidelity $F(T, \Delta\omega)$ as a function of probe pulse duration T for different values of $\Delta\omega$. We define the average fidelity as $\overline{F}(T) = \int_{-\infty}^{\infty} F(T, \Delta\omega) G(\Delta\omega) d\Delta\omega$, where $G(\Delta\omega)$ is the probability distribution of the random variable $\Delta\omega$. Spectral diffusion is often modeled as a Gaussian distribution [38], given by

$$G(\Delta\omega) = \frac{2}{\gamma_I}\sqrt{\frac{\ln 2}{\pi}} \exp\left(-4\ln 2\left(\frac{\Delta\omega}{\gamma_I}\right)^2\right) \tag{5.11}$$

where γ_I is the inhomogeneously broadened linewidth. We define the optimal fidelity as $\overline{F}_{opt} = \max_T[\overline{F}(T)]$.

The red solid line in Fig. 5.4 shows $\overline{F}_{opt}$ as a function of inhomogeneously broadened linewidth γ_I. In this calculation we ignore the effect of trion dephasing ($\gamma_d = 0$), and we set all other parameters the same as the ones used in the red solid line of Fig. 5.2(a). The fidelity remains very robust to inhomogeneously broadened linewidth, in contrast to the case with homogenously broadened linewidth. This result might be surprising at first, since with larger inhomogeneous linewidth, the contributions from those cases where the transition σ_1 and the cavity are detuned become more significant. For these detuned cases, the contrast of photon collection rate between the spin-up and spin-down states are lower than the resonant case, which might degrade the fidelity. To explain the robustness, we note that the detuned contributions also suppress the laser induced spin flip. The robustness of the fidelity over the emitter spectral diffusion makes this protocol very appealing for experimental realizations in the quantum dot system and many other solid-state

qubit systems.

5.3 Experimental demonstrations

5.3.1 Device characterization

To experimentally demonstrate spin readout using cavity QED, we utilize the same device as shown in Chapter 3, which is composed of a single charged InAs quantum dot coupled to a GaAs photonic crystal cavity. Here we apply a magnetic field along the Faraday geometry. In this configuration, the quantum dot exhibits an energy structure as shown in Fig. 1.2(a). Only transitions σ_+ and σ_- are optically allowed and coupled to the cavity.

We mount the sample in a closed-cycle cryostat with an integrated superconducting magnet system. The crystat cools the sample down to 3.6 K, while the magnet can apply magnetic fields of up to 9.2 T. We excite the sample and collect the reflected signal using a confocal microscope with an objective lens that has a numerical aperture of 0.8. We measure the collection efficiency of the objective lens to be 4.4% using the Stark shift of the quantum dot under cavity resonant excitation [90]. A single mode fiber spatially filters the collected signal to remove spurious surface reflection. We perform spectral measurements using a grating spectrometer with a spectral resolution of 7 GHz to perform spectral measurements. To measure the temporal properties of the signal we perform photon couting measurements using a Single Photon Counting Module (SPCM) with a time resolution of 800 ps., The detection efficiency of the photon counters is 30% at the device wavelength.

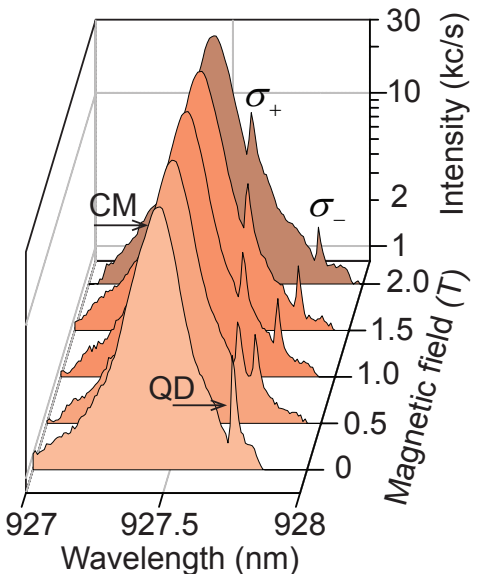

Figure 5.5: Cavity reflection spectrum at several different magnetic fields.

We first characterize the device by exciting the cavity with a broadband Light Emitting Diode (LED) that is polarized along the diagonal direction, and measuring the reflected signal along the anti-diagonal direction. The LED serves as a white light with emission in the wavelength range of 900 nm to 950 nm. Figure 5.5 shows the cavity reflection spectrum at several different magnetic fields. At 0 T, the spectrum shows a bright peak due to the cavity (labeled as CM) and a second peak due to the quantum dot (labeled as QD), which is red-detuned from the cavity resonance by 0.27 nm (94 GHz). By fitting the cavity peak measured at 0 T to a Lorentzian function, we determine the cavity energy decay rate to be $\kappa/2\pi = 33.2 \pm 0.6$ GHz. At higher magnetic field the quantum dot splits into two peaks, corresponding to the σ_+ and σ_- transitions shown in Fig. 1.2(a).

To measure the coupling strength between transition σ_+ and the cavity, we set

the magnetic field to 3.7 T where transition σ_+ is resonant with the cavity mode, and transition σ_- is largely detuned. This will also be the condition for us to perform spin readout. We probe the cavity reflectivity using a narrow bandwidth laser ($<$ 300 kHz) instead of a broadband LED, and use a second narrow bandwidth laser to optically pump the spin to the spin-up state by resonantly driving transition σ_- [68–70]. The blue circles in Fig. 5.6(a) show the reflected probe intensity as we tune the probe frequency across the cavity mode. By fitting the spectrum to a theoretical model (blue solid line), we determine the coupling strength between the σ_+ transition and the cavity to be $g/2\pi = 10.3 \pm 0.1$ GHz. The coupling strength satisfies the condition $g > \kappa/4$, demonstrating that we are operating in the strong coupling regime. Fig. 5.6(b) shows the case where we measure the cavity reflection spectrum along the diagonal polarization basis (same polarization as the incident field).

5.3.2 Time resolved spin-dependent reflectivity

To demonstrate spin-dependent cavity reflectivity, we use a pump-probe sequence as shown in Fig. 5.7. The pump pulse prepares the spin to either the spin-up or the spin-down state by resonantly pumping either the σ_- or σ_+ transition. The probe pulse is always resonant with the σ_+ transition and the cavity mode. We set the polarization of the incident probe pulse to be in the diagonal direction, and we measure the reflected probe intensity along the same polarization basis.

Figure 5.8 shows the intensity of the reflected probe pulse when the spin is

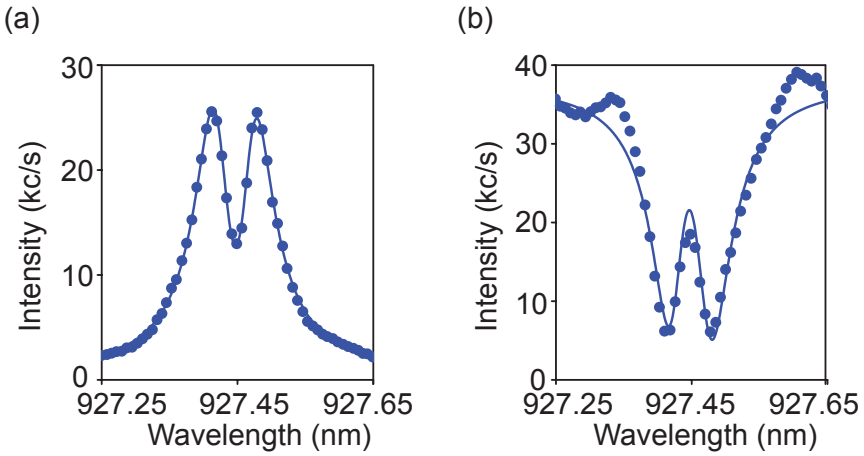

Figure 5.6: Cavity reflection spectrum at $B = 3.7$ T where transition σ_+ is resonant with the cavity. (a) Cross-polarized cavity reflection spectrum with a pumping laser that is resonant with transition σ_-. (b) Co-polarized cavity reflection spectrum with a pumping laser that is resonant with transition σ_-. In both (a) and (b), blue circles show measured data, while blue solid lines show calculated spectrum.

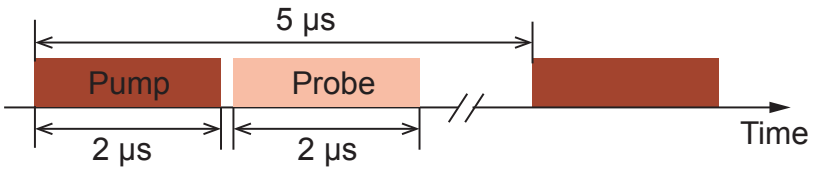

Figure 5.7: Pulse sequence that we utilize to demonstrate spin-dependent cavity reflectivity and spin readout.

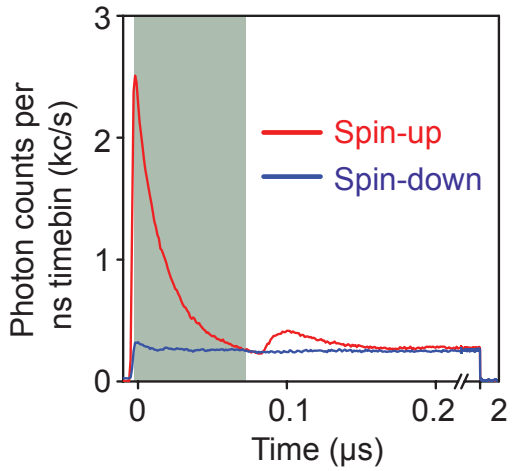

Figure 5.8: Intensity of the reflected probe pulse. The blue and red solid line shows the case when the spin is initialized in the spin-down and spin-up state respectively.

initialized to the spin-up state (blue line) and spin-down state (red line) respectively. The reflection intensity is much stronger for the spin-up case compared to the spin-down case, which enables us to distinguish the spin states from the measured intensity. For the spin-up case, the reflected signal exponentially decays to the background level due to the probe induced spin flip, which sets an upper limit for the detection window that we can use to collect photons.

5.3.3 Cavity enhanced spin readout fidelity

To perform spin readout, we assign the spin state as spin-up if we detect no photons within a detection window, and spin-down if we detect one (or more) photons. Since there is no a-priori knowledge about the spin-state, the average spin readout fidelity is given by $F = 0.5(p_\uparrow + p_\downarrow)$, where $p_\uparrow$ is the probability of detecting

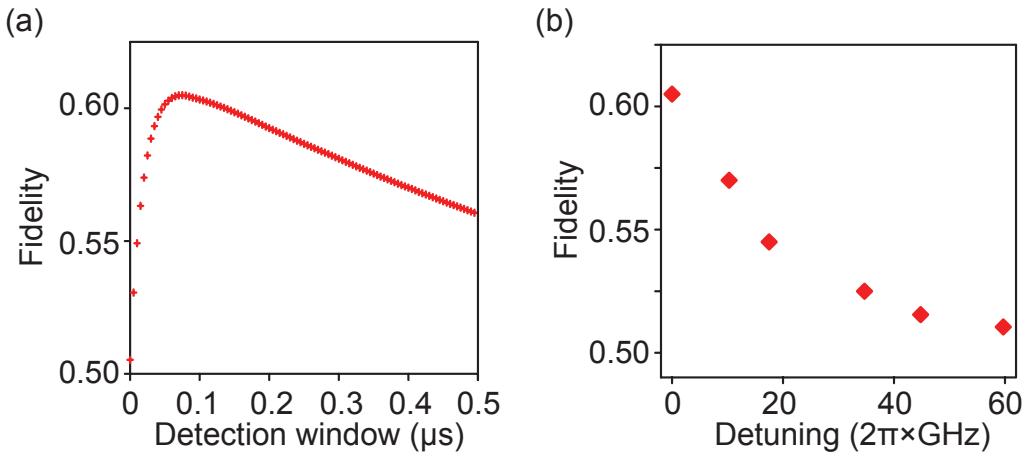

Figure 5.9: Measured fidelity of the spin readout operation. (a) Measured spin readout fidelity as a function of the detection window. (b) Measured spin readout fidelity as a function of the detuning between transition σ_+ and the cavity.

zero photons for the spin-up state, and $p_\downarrow$ is the probability of detecting at least one photon for the spin-down state.

The fidelity depends on the length of the detection window. Figure 5.9(a) shows the measured fidelity as a function of the detection window. The fidelity initially grows with longer detection window, because the probability of detecting at least one photon for the bright state increases. At even longer detection window the fidelity achieves a maximum and begins to decline because the probe pulse induces a spin-flip. We achieve the maximal fidelity of 0.61 with a detection window of 75 ns. This detection window is indicated as the grey area in Fig. 5.8.

To show the cavity enhancement of the spin readout, we introduce detuning between the cavity and the transition σ_+ by reducing the magnetic field, and repeat the same measurements for several different detuning conditions. The red circles

in Fig. 5.9(b) shows the measured optimal fidelity (optimized at the best detection window for each detuning) as a function of detuning between the transition σ_+ and the cavity. The fidelity rapidly drops as we increase the detuning and achieves the maximum at the resonance condition, demonstrating that the cavity is enhancing the spin readout.

We note that despite the cavity enhancement, the spin readout fidelity that we achieve is still lower than the best value that other groups have reported for spin readout of a bare quantum dot in the Faraday configuration using fluorescence light detection [73]. The major reason is that the particular dot we measured shows a very large non-radiative decay rate for the optical forbidden transition $|\Uparrow\rangle \rightarrow |\downarrow\rangle$, which is measured to be $\gamma_{nr}/2\pi = 49.4 \pm 1.8$ MHz by measuring the optical induced spin-flip time at the saturation power [72]. This value is about 100 times larger than the value reported previously [72, 73]. We calculate the maximum fidelity that one could achieve using fluorescence light detection for this dot to be 0.505 (assuming the same overall photon detection efficiency). This fundamental limit is much lower than the cavity enhanced value. We do not have clear evidence why the particular dot shows such a dramatically large decay rate for the optically forbidden transition. It could be caused by larger heavy-hole-light-hole (LH-HH) mixing.

5.4 Discussions

In conclusion, we have proposed a protocol for single-shot optical readout of a qubit that does not possess a good cycling transition. This protocol is broadly

applicable to many qubit systems including quantum dot spins, fluorine impurities in CdTe, silicon vacancy centers, and may also be useful for lots of new and emerging qubit systems that are still under developed. We have also experimentally demonstrated this approach using a strongly coupled quantum dot and photonic crystal cavity system. We show that the cavity enhanced spin readout fidelity breaks the fundamental limit for using resonance fluorescence from a bare quantum dot.

While we have shown optical spin readout that is strongly enhanced by a cavity, our experimental results have not yet reached the single-shot regime. Based on the theoretical calculation, single-shot regime could be achieved by improving the overall photon collection efficiency, which could be achieved by using cavity designs that enhance directional emission [126–128] or using single photon detectors that have higher quantum efficiency [132]. We can also improve the spin readout fidelity by improving the system cooperativity, which could be achieved by using cavities with smaller mode volume [133, 134] or higher quality factor [125, 135, 136]. Our theoretical calculation has shown the feasibility of implementing this protocol on a charged quantum dot in the Voigt configuration, which could simultaneously enable all-optical coherent spin manipulation and single-shot optical readout of the quantum dot spin, an important step towards quantum dot spin based quantum information processing [137, 138]. Our results show how tailoring light-matter interactions opens up new possibilities for processing quantum information with higher speed and accuracy.

Chapter 6: Strain tuning techniques for quantum dot based cavity QED system

As demonstrated in previous chapters, semiconductor quantum dots coupled to photonic crystal cavities offer a robust and scalable platform for studying cavity QED in a solid state device. The high quality factor and small mode volume of photonic crystal cavities, coupled with the large oscillator strength of quantum dots, enable light-matter interactions in the strong coupling regime [34]. This regime is a prerequisite for applications such as cavity reflectivity control [38], ultrafast optical switch [39–41], single photon level nonlinearities [42–44], non-classical light generation [45, 46], and spin-exciton quantum logic operations [47].

The study of quantum dots coupled to photonic crystal cavities often requires the ability to tune the quantum dot exciton energy *in-situ*. Tuning compensates for spectral mismatch between the quantum dot exciton energy and the cavity resonant frequency, and also provides control over the interaction strength between the two systems. The quantum dot exciton energy can be tuned by various means such as changing the sample temperature [34, 38], applying an AC Stark shift [90], utilizing the quantum confined Stark effect [139], or applying a magnetic field [140–142]. Temperature tuning and AC Stark effect can broaden the linewidth of the quantum

dot through phonon scattering [143] or excitation induced dephasing [144–147]. The quantum confined Stark effect does not suffer from these drawbacks but can quench quantum dot emission at high electric fields due to separation of the electron and hole wavefunctions [148]. Magnetic field tuning can reduce the coupling strength between the quantum dot and the cavity by changing the polarization of the emitted light and by magnetic field induced carrier confinement which lowers the quantum dot oscillator strength [140].

Strain tuning is an alternate method for tuning quantum dots [149–160]. In this method strain modifies the confinement of electrons and holes, thereby changing their Coulomb interaction strength [151]. Strain tuning can reversibly shift the quantum dot exciton energy without affecting its emission linewidth or intensity [151], and can achieve a very large tuning range of up to 20 meV [160]. These advantages make strain a promising method for tuning quantum dots coupled to optical cavities. Strain tuning of a single quantum dot strongly coupled to a microdisk cavity has been previously reported [158]. However, applying strain to a photonic crystal cavity can be challenging because these structures are supported on suspended membranes. Recently, several methods to tune the resonances of photonic crystal cavity modes with strain have been demonstrated [100, 161]. These techniques open up the possibility for strain tuning quantum dots in a photonic crystal device.

In this Chapter, we demonstrate reversible *in-situ* strain tuning of a quantum dot strongly coupled to a photonic crystal cavity. We achieve an average strain induced shift of 0.45 nm and demonstrate anti-crossing of a quantum dot and a photonic crystal cavity mode. We show that inside the cavity membrane, quantum

dots exhibit large fluctuations in the strain induced shift as compared to those in the bulk, and also shift in the opposite direction. These results indicate that the strain in the membrane region is very different from that of the bulk. We also demonstrate that the cavity mode resonance shifts by an amount that is 5.8 times smaller than the typical quantum dot shift. Thus, the quantum dot can be tuned over an appreciable range with only a small change to the cavity resonance.

This chapter is organized as follows. Section 6.1 discusses device characterization. In Section 6.2 and 6.3, we report the effect of the strain on quantum dots and cavity mode respectively. Section 6.4 concludes the discussions of this Chapter.

6.1 Device characterization

Figure 6.1 shows a schematic of the sample mount used to perform strain tuning. We utilize the approach demonstrated by Luxmoore et. al. [100] for reversible strain tuning of a photonic crystal cavity mode. An L-shaped copper holder is mounted on the cold finger of a continuous flow liquid helium cryostat. The sample and a piezo-electric actuator are mounted in parallel on the holder, with the direction of the applied stress (y-axis shown in the figure) aligned along the row defect of the photonic crystal cavities. The actuator is made of a 530 μm thick $[Pb(Mg_{1/3}Nb_{2/3})O_3]_{0.68}[PbTiO_3]_{0.32}$ (PMN-PT) substrate with gold coat on both the top and bottom surface to create an electrical contact. The PMN-PT substrate is poled in the [011] direction such that an out-of-plane electric field induces an anisotropic in-plane strain in the substrate. We use the convention that a posi-

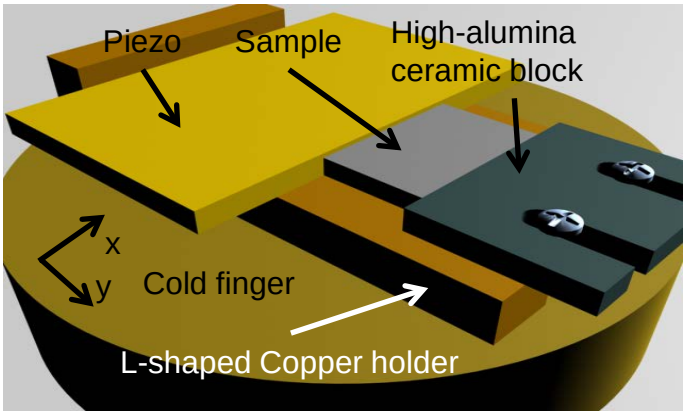

Figure 6.1: Schematic diagram of the experimental setup used to apply strain to the sample.

tive electric field results in expansion (contraction) in the y-direction (x-direction). The device and mounting stage are cooled down to a temperature below 40 K for photoluminescence measurements.

We excite the sample with a continuous wave Ti:sapphire laser tuned to a wavelength of 780 nm and collect the emitted photoluminescence using a confocal microscope with a 0.7 numerical aperture objective lens. The spectrum of the collected signal is measured using a grating spectrometer with a resolution of 0.02 nm. Figure 6.2(a) shows the emission spectrum from a photonic crystal cavity which exhibits a bright peak at the cavity resonant frequency. We fit this peak to a Lorentzian function and determine a cavity quality factor of 12,000 (corresponding to a cavity decay rate of $\kappa/2\pi = 27.3$ GHz). Figure 6.2(b) shows a temperature scan of the photoluminescence spectrum where a fixed electric field of 11.25 kV/cm was applied to the piezo during the temperature scan. A quantum dot line (labeled

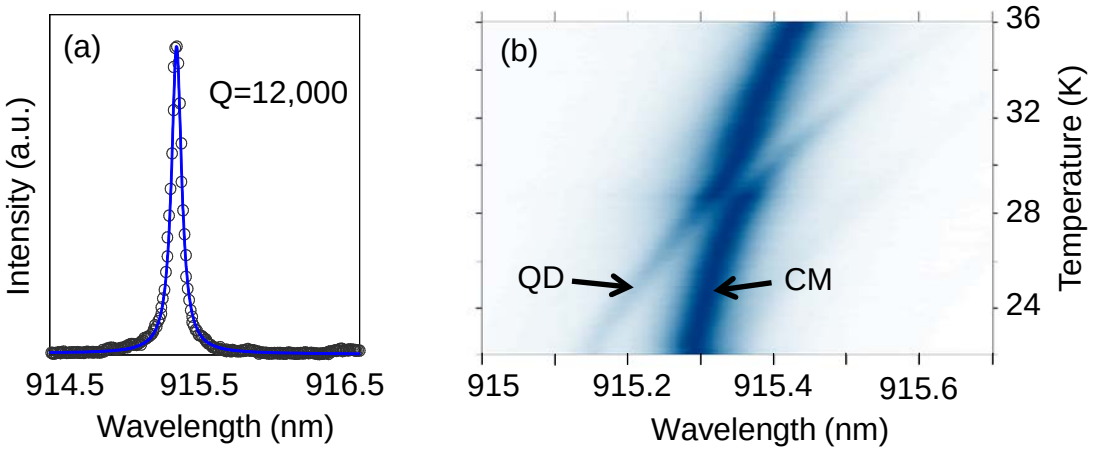

Figure 6.2: Device characterization with photoluminescence. (a) Photoluminescence spectrum of a photonic crystal cavity at 30 K showing a quality factor of 12,000. The black circles correspond to measured spectrum and the blue solid line shows Lorentzian fit. (b) Photoluminescence spectrum of strongly coupled quantum dot and cavity as a function of temperature.

QD) anti-crosses with the cavity mode (labeled as CM), indicating strong coupling. Note that we cannot determine whether the quantum dot resonance corresponds to a neutral or charged exciton emission from the spectral data shown in Figure 6.2(b). However, because the neutral, charged, and bi-exciton lines all experience nearly identical behavior under strain [151, 159], the exact nature of the exciton emission does not affect our results.

6.2 The effects of strain on quantum dots

To demonstrate strain tuning, we perform photoluminescence measurement on the same device at a fixed temperature of 30 K while sweeping the electric field applied to the piezo from zero to 15 kV/cm and then back to zero. Figure 6.3(a)

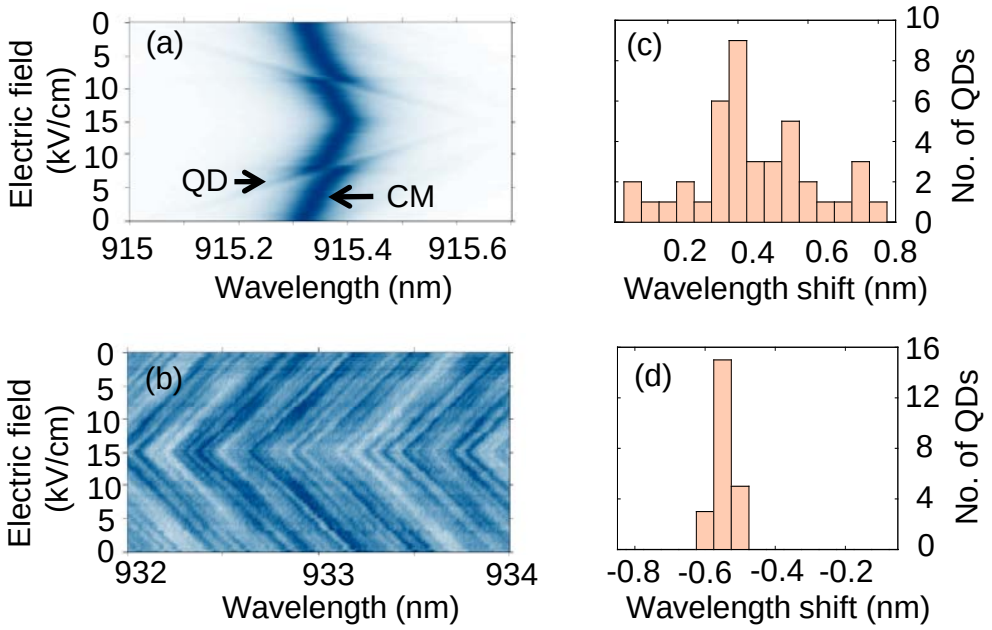

Figure 6.3: The effect of strain on quantum dots. (a) Photoluminescence of the cavity shown in Fig. 6.2(b) as a function of electric field. (b) Photoluminescence of bulk wafer containing several quantum dots as a function of electric field. (c) Histogram of the wavelength shift for 41 different quantum dots embedded in 5 different photonic crystal cavities for an electric field of 15 kV/cm. (d) Histogram of the wavelength shift for 23 different bulk quantum dots using an electric field of 15 kV/cm. The sample temperature is fixed at 30 K for all above measurements.

shows the measured spectrum as a function of applied electric field. As the electric field increases, the quantum dot red-shifts across the cavity resonance, and becomes resonant at an applied field of 7.8 kV/cm. We observe a clear anti-crossing as the quantum dot exciton energy is tuned through the cavity resonance due to strong coupling. The quantum dot exciton energy returns to its original value when the field is reduced back to zero, indicating that the strain tuning process is reversible.

The redshift of the quantum dot suggests a tensile strain distribution in the center of the cavity, which is opposite to the expected direction because we are ap-

plying compressive stress. For comparison, Fig. 6.3(b) plots the photoluminescence as a function of electric field in the bulk region of the sample, far away from all fabricated devices. Multiple quantum dot lines appear in the measured spectrum. In contrast to the photonic crystal membrane, all bulk quantum dots experience a blueshift with increasing electric field, consistent with previous studies of quantum dots under compressive stress [149]. Thus, there is a large difference in the strain distribution inside the cavity membrane as compared to the bulk material.

To gain a further insight into the strain distribution inside the cavity membrane, we measure the wavelength shift for 41 different quantum dots at the center of 5 different cavities using an electric field of 15 kV/cm and plot the histogram in Fig. 6.3(c). All quantum dots exhibit a redshift, with an average value of $\Delta\lambda_{cav} =$ 0.45 nm, equal to 6 cavity linewidth, but there is large variations in the shift. We note that although the magnitude of the strain shift can vary from dot to dot, for each individual dot the tuning is highly repeatable and reversible over many cycles of the experiment. In contrast, Fig. 6.3(d) plots a histogram of the wavelength shift at the maximum electric field for 23 individual quantum dots in the bulk far away from all cavities. The histogram shows a very narrow distribution indicating that the bulk exhibits compressive strain with a relatively uniform strain distribution. We determine a maximum shift of $\Delta\lambda_{bulk} =$ -0.52 nm (averaged over all the quantum dots) at the maximum electric field. The narrow distribution for bulk quantum dots suggests that the variability in tuning range for quantum dots in the membrane is largely due to strain variations at different locations inside the membrane. We also speculate that the unexpected strain direction in the cavity may be due to bowing

or warping of the membrane, which may depend on complex factors such as size of undercut and shape of the photonic crystal.

6.3 The effect of strain on a cavity mode

The strain dependent spectrum in Fig. 6.3(a) shows that, in addition to tuning of the quantum dots, the cavity mode also exhibits a small redshift. The direction of cavity mode shift suggests a tensile strain inside the cavity membrane [161], consistent with the shift of the quantum dots. Because the strain induced cavity shift is in the same direction as the quantum dot shift, it reduces the effective tuning range of the coupled quantum dot and cavity system. Figure 6.4(a) shows the photoluminescence spectrum of a bare cavity mode as a function of electric field at 30 K (these measurements were performed on a different device). By fitting the emission spectrum at an electric field of zero and 15 kV/cm to a Lorentzian function (see Fig. 6.4(b)), we determine a spectral redshift of 0.078 nm. This shift is 5.8 times smaller than the average quantum dot shift in the cavity, indicating that the cavity shift is a small effect in this system.

6.4 Discussions

In conclusion, we demonstrated *in-situ* strain tuning of a quantum dot strongly coupled to a photonic crystal cavity. The average tuning range for quantum dots within the cavity is about 6 cavity linewidth. This tuning range could be further extended by applying higher electric field to the piezo. In our experiment we use

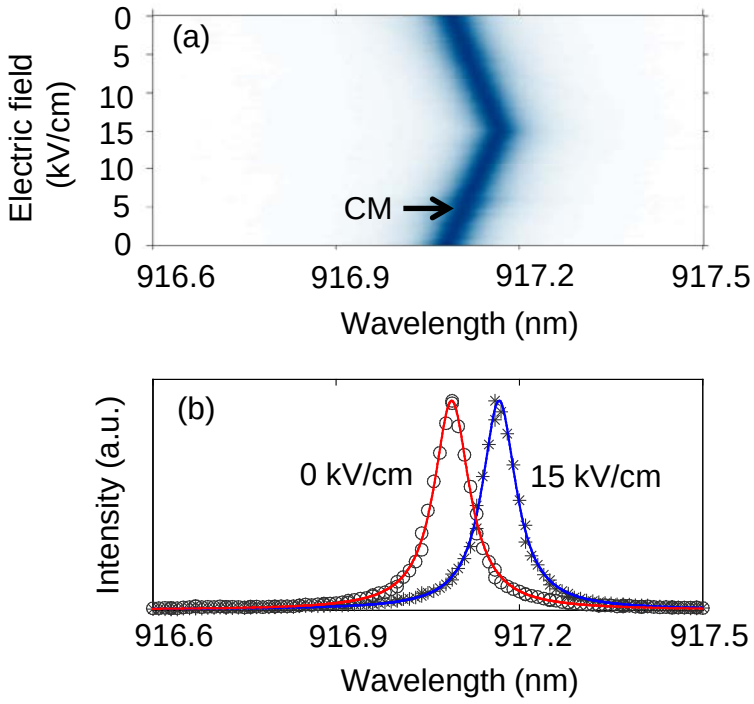

Figure 6.4: The effect of strain on a cavity mode. (a) Photoluminescence spectrum of a cavity mode as a function of applied electric field. (b) Measured cavity spectrum at an applied electric field of zero (black circles) and 15 kV/cm (black stars). The red (blue) solid line shows Lorentzian fit to the spectrum at an electric field of zero (15 kV/cm).

an electric field range of 15 kV/cm due to limited range of our voltage source, but previous works have applied electric field ranging as large as 80 kV/cm and have attained highly repeatable results [160]. Methods to improve strain transfer into the sample such as using a stiffer bracket and a smaller piece of substrate may also improve tuning range. Finally, it is also possible to use a different type of quantum dots that are more sensitive to strain [159, 162]. The current device implementation can be adapted to apply strain locally to individual cavities using micro-fabricated piezoelectric micro-electro-mechanical structures. The combination of local strain tuning of quantum dots with photonic crystals provides a promising path towards integrated nonlinear photonic devices for ultra-low power opto-electronics and quantum information processing on a chip.

Chapter 7: Conclusions and future directions

In this thesis, we have demonstrated a quantum interface between a single solid-state spin and a photon using a nanophotonic cavity QED system. We show that the spin-photon quantum interface enables lots of important applications in quantum information processing, including spin-photon quantum phase switching, deterministic spin-photon entanglement generation, and high-fidelity optical spin readout. In addition, the demonstrated device monolithically combines spins with strongly interacting nanophotonic structures on a single semiconductor chip, which may have many beneficial properties for future integration and scalability.

One important aspects of the future works is to improve the performance of the device. Smaller mode-volume cavity designs could enable higher switching fidelity and spin readout fidelity by improving the system cooperativity [133, 134]. Using delta-doping layers [23] or active charge stabilization [50] could further improve the spin state preparation fidelity. Our results can also be directly applied in waveguide integrated devices that are more conducive to on-chip integration and can exhibit similar strong light-matter interactions [81]. In such on-chip implementations, waveguide losses create further challenges by degrading the cavity quality factor, which would reduce the cooperativity. Waveguide-coupled devices would

therefore require higher bare cavity quality factor to ensure that the light remains on the chip. Past work has demonstrated a quality factor exceeding 50,000 using GaAs photonic crystal cavities operating at near-infrared wavelengths [135], and quality factor exceeding 250,000 in cavities operating at a longer wavelength [136], which could potentially enable both efficient on-chip coupling and high cooperativity. Employing regulated quantum dot growth techniques [163, 164] in conjunction with local frequency tuning [90] could further open up the possibility to integrate multiple quantum dot spins on a single semiconductor chip.

The ultimate direction for our research is to construct integrated quantum photonic circuits and on-chip quantum processors using the nanophotonic platform with solid-state spins embedded. The results reported in this thesis utilized single quantum dot spins as the qubit system. But our results are applicable to a broad range of solid-state emitters and solid-state qubit systems, including other species of quantum dots [165], color centers [166, 167], rare earth ions [168], defects in 2D materials [169–172] and etc. In addition, by interconnecting each solid-state spin with a single photon, a hybrid integrated quantum circuits composed of different types of qubit systems might be feasible, where the interactions between different qubits are mediated via photons. This hybrid configuration might benefit from the combined advantages of each individual qubit systems.

In conclusion, we note that numerous fascinating research possibilities are ahead towards the ultimate realization of a chip-integrated quantum processor or a quantum network. We hope that our work contribute only a small portion of what will be achieved in the future.

Bibliography

[1] Juan Ignacio Cirac, Peter Zoller, H Jeff Kimble, and Hideo Mabuchi. Quantum state transfer and entanglement distribution among distant nodes in a quantum network. *Physical Review Letters*, 78(16):3221, 1997.

[2] H Jeff Kimble. The quantum internet. *Nature*, 453(7198):1023–1030, 2008.

[3] JI Cirac, AK Ekert, SF Huelga, and C Macchiavello. Distributed quantum computation over noisy channels. *Physical Review A*, 59(6):4249, 1999.

[4] Jaeyoon Cho and Hai-Woong Lee. Generation of atomic cluster states through the cavity input-output process. *Physical review letters*, 95(16):160501, 2005.

[5] Stephan Ritter, Christian Nölleke, Carolin Hahn, Andreas Reiserer, Andreas Neuzner, Manuel Uphoff, Martin Mücke, Eden Figueroa, Joerg Bochmann, and Gerhard Rempe. An elementary quantum network of single atoms in optical cavities. *Nature*, 484(7393):195–200, 2012.

[6] Jürgen Volz, Roger Gehr, Guilhem Dubois, Jérôme Estève, and Jakob Reichel. Measurement of the internal state of a single atom without energy exchange. *Nature*, 475(7355):210–213, 2011.

[7] Andreas Reiserer, Stephan Ritter, and Gerhard Rempe. Nondestructive detection of an optical photon. *Science*, 342(6164):1349–1351, 2013.

[8] TG Tiecke, Jeffrey Douglas Thompson, Nathalie Pulmones de Leon, LR Liu, V Vuletić, and Mikhail D Lukin. Nanophotonic quantum phase switch with a single atom. *Nature*, 508(7495):241–244, 2014.

[9] L-M Duan and HJ Kimble. Scalable photonic quantum computation through cavity-assisted interactions. *Physical review letters*, 92(12):127902, 2004.

[10] Andreas Reiserer, Norbert Kalb, Gerhard Rempe, and Stephan Ritter. A quantum gate between a flying optical photon and a single trapped atom. *Nature*, 508(7495):237–240, 2014.

[11] Dirk Englund, Andrei Faraon, Bingyang Zhang, Yoshihisa Yamamoto, and Jelena Vučković. Generation and transfer of single photons on a photonic crystal chip. *Optics Express*, 15(9):5550–5558, 2007.

[12] Andrei Faraon, Arka Majumdar, Dirk Englund, Erik Kim, Michal Bajcsy, and Jelena Vučković. Integrated quantum optical networks based on quantum dots and photonic crystals. *New Journal of Physics*, 13(5):055025, 2011.

[13] A Imamog, David D Awschalom, Guido Burkard, David P DiVincenzo, Daniel Loss, M Sherwin, A Small, et al. Quantum information processing using quantum dot spins and cavity qed. *Physical Review Letters*, 83(20):4204, 1999.

[14] Edo Waks and Jelena Vuckovic. Dipole induced transparency in drop-filter cavity-waveguide systems. *Physical review letters*, 96(15):153601, 2006.

[15] Darrick E Chang, Anders S Sørensen, Eugene A Demler, and Mikhail D Lukin. A single-photon transistor using nanoscale surface plasmons. *Nature Physics*, 3(11):807–812, 2007.

[16] CY Hu, A Young, JL OBrien, WJ Munro, and JsG Rarity. Giant optical faraday rotation induced by a single-electron spin in a quantum dot: applications to entangling remote spins via a single photon. *Physical Review B*, 78(8):085307, 2008.

[17] Cristian Bonato, Florian Haupt, Sumant SR Oemrawsingh, Jan Gudat, Dapeng Ding, Martin P van Exter, and Dirk Bouwmeester. Cnot and bell-state analysis in the weak-coupling cavity qed regime. *Physical review letters*, 104(16):160503, 2010.

[18] Ying Li, Leandro Aolita, Darrick E Chang, and Leong Chuan Kwek. Robust-fidelity atom-photon entangling gates in the weak-coupling regime. *Physical review letters*, 109(16):160504, 2012.

[19] Kae Nemoto, Michael Trupke, Simon J Devitt, Ashley M Stephens, Burkhard Scharfenberger, Kathrin Buczak, Tobias Nöbauer, Mark S Everitt, Jörg Schmiedmayer, and William J Munro. Photonic architecture for scalable quantum information processing in diamond. *Physical Review X*, 4(3):031022, 2014.

[20] Xiaodong Xu, Wang Yao, Bo Sun, Duncan G Steel, Allan S Bracker, Daniel Gammon, and LJ Sham. Optically controlled locking of the nuclear field via coherent dark-state spectroscopy. *Nature*, 459(7250):1105–1109, 2009.

[21] David Press, Kristiaan De Greve, Peter L McMahon, Thaddeus D Ladd, Benedikt Friess, Christian Schneider, Martin Kamp, Sven Höfling, Alfred Forchel, and Yoshihisa Yamamoto. Ultrafast optical spin echo in a single quantum dot. *Nature Photonics*, 4(6):367–370, 2010.

[22] J Berezovsky, MH Mikkelsen, NG Stoltz, LA Coldren, and DD Awschalom. Picosecond coherent optical manipulation of a single electron spin in a quantum dot. *Science*, 320(5874):349–352, 2008.

[23] David Press, Thaddeus D Ladd, Bingyang Zhang, and Yoshihisa Yamamoto. Complete quantum control of a single quantum dot spin using ultrafast optical pulses. *Nature*, 456(7219):218–221, 2008.

[24] Erik D Kim, Katherine Truex, Xiaodong Xu, Bo Sun, DG Steel, AS Bracker, D Gammon, and LJ Sham. Fast spin rotations by optically controlled geometric phases in a charge-tunable inas quantum dot. *Physical review letters*, 104(16):167401, 2010.

[25] Kristiaan De Greve, Peter L McMahon, David Press, Thaddeus D Ladd, Dirk Bisping, Christian Schneider, Martin Kamp, Lukas Worschech, Sven Höfling, Alfred Forchel, et al. Ultrafast coherent control and suppressed nuclear feedback of a single quantum dot hole qubit. *Nature Physics*, 7(11):872–878, 2011.

[26] Timothy Mark Godden, JH Quilter, AJ Ramsay, Yanwen Wu, P Brereton, SJ Boyle, IJ Luxmoore, J Puebla-Nunez, AM Fox, and MS Skolnick. Coherent optical control of the spin of a single hole in an inas/gaas quantum dot. *Physical review letters*, 108(1):017402, 2012.

[27] Yu He, Yu-Ming He, Y-J Wei, X Jiang, M-C Chen, F-L Xiong, Y Zhao, Christian Schneider, Martin Kamp, Sven Höfling, et al. Indistinguishable tunable single photons emitted by spin-flip raman transitions in ingaas quantum dots. *Physical review letters*, 111(23):237403, 2013.

[28] Kristiaan De Greve, Leo Yu, Peter L McMahon, Jason S Pelc, Chandra M Natarajan, Na Young Kim, Eisuke Abe, Sebastian Maier, Christian Schneider, Martin Kamp, et al. Quantum-dot spin-photon entanglement via frequency downconversion to telecom wavelength. *Nature*, 491(7424):421–425, 2012.

[29] WB Gao, Parisa Fallahi, Emre Togan, Javier Miguel-Sánchez, and Atac Imamoglu. Observation of entanglement between a quantum dot spin and a single photon. *Nature*, 491(7424):426–430, 2012.

[30] JR Schaibley, AP Burgers, GA McCracken, L-M Duan, PR Berman, DG Steel, AS Bracker, D Gammon, and LJ Sham. Demonstration of quantum entanglement between a single electron spin confined to an inas quantum dot and a photon. *Physical review letters*, 110(16):167401, 2013.

[31] Kristiaan De Greve, Peter L McMahon, Leo Yu, Jason S Pelc, Cody Jones, Chandra M Natarajan, Na Young Kim, Eisuke Abe, Sebastian Maier, Christian Schneider, et al. Complete tomography of a high-fidelity solid-state entangled spin–photon qubit pair. *Nature communications*, 4, 2013.

[32] WB Gao, P Fallahi, E Togan, A Delteil, YS Chin, J Miguel-Sanchez, and A Imamoğlu. Quantum teleportation from a propagating photon to a solid-state spin qubit. *Nature communications*, 4, 2013.

[33] Aymeric Delteil, Zhe Sun, Wei-bo Gao, Emre Togan, Stefan Faelt, and Ataç Imamoglu. Generation of heralded entanglement between distant hole spins. *Nature Physics*, 2015.

[34] Tomoyuki Yoshie, Axel Scherer, J Hendrickson, G Khitrova, HM Gibbs, G Rupper, C Ell, OB Shchekin, and DG Deppe. Vacuum rabi splitting with a single quantum dot in a photonic crystal nanocavity. *Nature*, 432(7014):200–203, 2004.

[35] JP Reithmaier, G Sek, A Löffler, C Hofmann, S Kuhn, S Reitzenstein, LV Keldysh, VD Kulakovskii, TL Reinecke, and A Forchel. Strong coupling in a single quantum dot–semiconductor microcavity system. *Nature*, 432(7014):197–200, 2004.

[36] Emmanuelle Peter, Pascale Senellart, David Martrou, Aristide Lemaître, J Hours, JM Gérard, and Jacqueline Bloch. Exciton-photon strong-coupling regime for a single quantum dot embedded in a microcavity. *Physical review letters*, 95(6):067401, 2005.

[37] Kevin Hennessy, Antonio Badolato, M Winger, D Gerace, Mete Atatüre, S Gulde, S Fält, Evelyn L Hu, and A Imamoğlu. Quantum nature of a strongly coupled single quantum dot–cavity system. *Nature*, 445(7130):896–899, 2007.

[38] Dirk Englund, Andrei Faraon, Ilya Fushman, Nick Stoltz, Pierre Petroff, and Jelena Vučković. Controlling cavity reflectivity with a single quantum dot. *Nature*, 450(7171):857–861, 2007.

[39] Dirk Englund, Arka Majumdar, Michal Bajcsy, Andrei Faraon, Pierre Petroff, and Jelena Vučković. Ultrafast photon-photon interaction in a strongly coupled quantum dot-cavity system. *Physical review letters*, 108(9):093604, 2012.

[40] Ranojoy Bose, Deepak Sridharan, Hyochul Kim, Glenn S Solomon, and Edo Waks. Low-photon-number optical switching with a single quantum dot coupled to a photonic crystal cavity. *Physical review letters*, 108(22):227402, 2012.

[41] Thomas Volz, Andreas Reinhard, Martin Winger, Antonio Badolato, Kevin J Hennessy, Evelyn L Hu, and Ataç Imamoğlu. Ultrafast all-optical switching by single photons. *Nature Photonics*, 6(9):605–609, 2012.

[42] Kartik Srinivasan and Oskar Painter. Linear and nonlinear optical spectroscopy of a strongly coupled microdisk–quantum dot system. *Nature*, 450(7171):862–865, 2007.

[43] Ilya Fushman, Dirk Englund, Andrei Faraon, Nick Stoltz, Pierre Petroff, and Jelena Vučković. Controlled phase shifts with a single quantum dot. *Science*, 320(5877):769–772, 2008.

[44] Dario Gerace, Hakan E Türeci, Atac Imamoglu, Vittorio Giovannetti, and Rosario Fazio. The quantum-optical josephson interferometer. *Nature Physics*, 5(4):281–284, 2009.

[45] Andrei Faraon, Ilya Fushman, Dirk Englund, Nick Stoltz, Pierre Petroff, and Jelena Vučković. Coherent generation of non-classical light on a chip via photon-induced tunnelling and blockade. *Nature Physics*, 4(11):859–863, 2008.

[46] Kai Müller, Armand Rundquist, Kevin A Fischer, Tomas Sarmiento, Konstantinos G Lagoudakis, Yousif A Kelaita, Carlos Sánchez Muñoz, Elena del Valle, Fabrice P Laussy, and Jelena Vučković. Coherent generation of nonclassical light on chip via detuned photon blockade. *Physical review letters*, 114(23):233601, 2015.

[47] Hyochul Kim, Ranojoy Bose, Thomas C Shen, Glenn S Solomon, and Edo Waks. A quantum logic gate between a solid-state quantum bit and a photon. *Nature Photonics*, 7(5):373–377, 2013.

[48] MT Rakher, NG Stoltz, LA Coldren, PM Petroff, and D Bouwmeester. Externally mode-matched cavity quantum electrodynamics with charge-tunable quantum dots. *Physical review letters*, 102(9):097403, 2009.

[49] Konstantinos G Lagoudakis, Kevin Fischer, Tomas Sarmiento, Arka Majumdar, Armand Rundquist, Jesse Lu, Michal Bajcsy, and Jelena Vučković. Deterministically charged quantum dots in photonic crystal nanoresonators for efficient spin–photon interfaces. *New Journal of Physics*, 15(11):113056, 2013.

[50] Samuel G Carter, Timothy M Sweeney, Mijin Kim, Chul Soo Kim, Dmitry Solenov, Sophia E Economou, Thomas L Reinecke, Lily Yang, Allan S Bracker, and Daniel Gammon. Quantum control of a spin qubit coupled to a photonic crystal cavity. *Nature Photonics*, 7(4):329–334, 2013.

[51] Christophe Arnold, Justin Demory, Vivien Loo, Aristide Lemaître, Isabelle Sagnes, Mikhaïl Glazov, Olivier Krebs, Paul Voisin, Pascale Senellart, and Loïc Lanco. Macroscopic rotation of photon polarization induced by a single spin. *Nature communications*, 6, 2015.

[52] P. Androvitsaneas, A. B. Young, C. Schneider, S. Maier, M. Kamp, S. Höfling, S. Knauer, E. Harbord, C. Y. Hu, J. G. Rarity, and R. Oulton. Charged quantum dot micropillar system for deterministic light-matter interactions. *Phys. Rev. B*, 93:241409, Jun 2016.

[53] PM Petroff and SP DenBaars. Mbe and mocvd growth and properties of self-assembling quantum dot arrays in iii-v semiconductor structures. *Superlattices and Microstructures*, 15(1):15, 1994.

[54] Peter Lodahl, Sahand Mahmoodian, and Søren Stobbe. Interfacing single photons and single quantum dots with photonic nanostructures. *Reviews of Modern Physics*, 87(2):347, 2015.

[55] Jeppe Johansen, Søren Stobbe, Ivan S Nikolaev, Toke Lund-Hansen, Philip T Kristensen, Jørn M Hvam, Willem L Vos, and Peter Lodahl. Size dependence of the wavefunction of self-assembled inas quantum dots from time-resolved optical measurements. *Physical Review B*, 77(7):073303, 2008.

[56] Søren Stobbe, Jeppe Johansen, Philip Trøst Kristensen, Jørn Märcher Hvam, and Peter Lodahl. Frequency dependence of the radiative decay rate of excitons in self-assembled quantum dots: Experiment and theory. *Physical Review B*, 80(15):155307, 2009.

[57] Dirk Englund, David Fattal, Edo Waks, Glenn Solomon, Bingyang Zhang, Toshihiro Nakaoka, Yasuhiko Arakawa, Yoshihisa Yamamoto, and Jelena Vučković. Controlling the spontaneous emission rate of single quantum dots in a two-dimensional photonic crystal. *Physical review letters*, 95(1):013904, 2005.

[58] Egor A Muljarov and R Zimmermann. Dephasing in quantum dots: Quadratic coupling to acoustic phonons. *Physical review letters*, 93(23):237401, 2004.

[59] HD Robinson and BB Goldberg. Light-induced spectral diffusion in single self-assembled quantum dots. *Physical Review B*, 61(8):R5086, 2000.

[60] Arka Majumdar, Erik D Kim, and Jelena Vučković. Effect of photogenerated carriers on the spectral diffusion of a quantum dot coupled to a photonic crystal cavity. *Physical Review B*, 84(19):195304, 2011.

[61] IA Merkulov, Al L Efros, and M Rosen. Electron spin relaxation by nuclei in semiconductor quantum dots. *Physical Review B*, 65(20):205309, 2002.

[62] Bernhard Urbaszek, Xavier Marie, Thierry Amand, Olivier Krebs, Paul Voisin, Patrick Maletinsky, Alexander Högele, and Atac Imamoglu. Nuclear spin physics in quantum dots: An optical investigation. *Reviews of Modern Physics*, 85(1):79, 2013.

[63] M Bayer, G Ortner, O Stern, A Kuther, AA Gorbunov, A Forchel, Pawel Hawrylak, S Fafard, K Hinzer, TL Reinecke, et al. Fine structure of neutral and charged excitons in self-assembled in (ga) as/(al) gaas quantum dots. *Physical Review B*, 65(19):195315, 2002.

[64] David P DiVincenzo. The physical implementation of quantum computation. *Fortschritte der Physik*, 48(9-11):771–783, 2000.

[65] Kristiaan De Greve, David Press, Peter L McMahon, and Yoshihisa Yamamoto. Ultrafast optical control of individual quantum dot spin qubits. *Reports on Progress in physics*, 76(9):092501, 2013.

[66] C Emary, Xiaodong Xu, DG Steel, S Saikin, and LJ Sham. Fast initialization of the spin state of an electron in a quantum dot in the voigt configuration. *Physical review letters*, 98(4):047401, 2007.

[67] Xiaodong Xu, Yanwen Wu, Bo Sun, Qiong Huang, Jun Cheng, DG Steel, AS Bracker, D Gammon, C Emary, and LJ Sham. Fast spin state initialization in a singly charged inas-gaas quantum dot by optical cooling. *Physical review letters*, 99(9):097401, 2007.

[68] Miro Kroutvar, Yann Ducommun, Dominik Heiss, Max Bichler, Dieter Schuh, Gerhard Abstreiter, and Jonathan J Finley. Optically programmable electron spin memory using semiconductor quantum dots. *Nature*, 432(7013):81–84, 2004.

[69] Mete Atatüre, Jan Dreiser, Antonio Badolato, Alexander Högele, Khaled Karrai, and Atac Imamoglu. Quantum-dot spin-state preparation with near-unity fidelity. *Science*, 312(5773):551–553, 2006.

[70] Brian D Gerardot, Daniel Brunner, Paul A Dalgarno, Patrik Öhberg, Stefan Seidl, Martin Kroner, Khaled Karrai, Nick G Stoltz, Pierre M Petroff, and Richard J Warburton. Optical pumping of a single hole spin in a quantum dot. *Nature*, 451(7177):441–444, 2008.

[71] A Nick Vamivakas, Yong Zhao, Chao-Yang Lu, and Mete Atatüre. Spin-resolved quantum-dot resonance fluorescence. *Nature Physics*, 5(3):198–202, 2009.

[72] C-Y Lu, Y Zhao, AN Vamivakas, C Matthiesen, S Fält, A Badolato, and M Atatüre. Direct measurement of spin dynamics in inas/gaas quantum dots using time-resolved resonance fluorescence. *Physical Review B*, 81(3):035332, 2010.

[73] Aymeric Delteil, Wei-bo Gao, Parisa Fallahi, Javier Miguel-Sanchez, and Atac Imamoğlu. Observation of quantum jumps of a single quantum dot spin using submicrosecond single-shot optical readout. *Physical review letters*, 112(11):116802, 2014.

[74] J Berezovsky, MH Mikkelsen, O Gywat, NG Stoltz, LA Coldren, and DD Awschalom. Nondestructive optical measurements of a single electron spin in a quantum dot. *Science*, 314(5807):1916–1920, 2006.

[75] Mete Atatüre, Jan Dreiser, Antonio Badolato, and Atac Imamoglu. Observation of faraday rotation from a single confined spin. *Nature Physics*, 3(2):101–106, 2007.

[76] MH Mikkelsen, J Berezovsky, NG Stoltz, LA Coldren, and DD Awschalom. Optically detected coherent spin dynamics of a single electron in a quantum dot. *Nature Physics*, 3(11):770–773, 2007.

[77] David Lawren Reid Press. *Quantum Dot Spins and Microcavities for Quantum Information Processing*. PhD thesis, Stanford University, 2010.

[78] Tao Cai, Ranojoy Bose, Glenn S Solomon, and Edo Waks. Controlled coupling of photonic crystal cavities using photochromic tuning. *Applied Physics Letters*, 102(14):141118, 2013.

[79] Alexander Y Piggott, Konstantinos G Lagoudakis, Tomas Sarmiento, Michal Bajcsy, Gary Shambat, and Jelena Vučković. Photo-oxidative tuning of individual and coupled gaas photonic crystal cavities. *Optics express*, 22(12):15017–15023, 2014.

[80] Andrei Faraon, Edo Waks, Dirk Englund, Ilya Fushman, and Jelena Vučković. Efficient photonic crystal cavity-waveguide couplers. *Applied Physics Letters*, 90(7):073102, 2007.

[81] Ranojoy Bose, Deepak Sridharan, GS Solomon, and E Waks. Observation of strong coupling through transmission modification of a cavity-coupled photonic crystal waveguide. *Optics express*, 19(6):5398–5409, 2011.

[82] Yoshihiro Akahane, Takashi Asano, Bong-Shik Song, and Susumu Noda. Fine-tuned high-q photonic-crystal nanocavity. *Optics Express*, 13(4):1202–1214, 2005.

[83] Shuo Sun, Hyochul Kim, Glenn S Solomon, and Edo Waks. A quantum phase switch between a single solid-state spin and a photon. *Nature nanotechnology*, 11(6):539–544, 2016.

[84] Shuo Sun and Edo Waks. Deterministic generation of entanglement between a quantum-dot spin and a photon. *Physical Review A*, 90(4):042322, 2014.

[85] Shuo Sun and Edo Waks. Single-shot optical readout of a quantum bit using cavity quantum electrodynamics. *Phys. Rev. A*, 94:012307, Jul 2016.

[86] Shuo Sun, Hyochul Kim, Glenn S Solomon, and Edo Waks. Strain tuning of a quantum dot strongly coupled to a photonic crystal cavity. *Applied Physics Letters*, 103(15):151102, 2013.

[87] Daniel F Walls and Gerard J Milburn. *Quantum optics*. Springer Science & Business Media, 2007.

[88] S Hughes and H Kamada. Single-quantum-dot strong coupling in a semiconductor photonic crystal nanocavity side coupled to a waveguide. *Physical Review B*, 70(19):195313, 2004.

[89] Jung-Tsung Shen, Shanhui Fan, et al. Theory of single-photon transport in a single-mode waveguide. i. coupling to a cavity containing a two-level atom. *Physical Review A*, 79(2):023837, 2009.

[90] R Bose, D Sridharan, GS Solomon, and E Waks. Large optical stark shifts in semiconductor quantum dots coupled to photonic crystal cavities. *Applied Physics Letters*, 98(12):121109, 2011.

[91] AJ Ramsay. A review of the coherent optical control of the exciton and spin states of semiconductor quantum dots. *Semiconductor Science and Technology*, 25(10):103001, 2010.

[92] Deepak Sridharan and Edo Waks. Generating entanglement between quantum dots with different resonant frequencies based on dipole-induced transparency. *Physical Review A*, 78(5):052321, 2008.

[93] Edo Waks and Christopher Monroe. Protocol for hybrid entanglement between a trapped atom and a quantum dot. *Physical Review A*, 80(6):062330, 2009.

[94] CY Hu, WJ Munro, and JG Rarity. Deterministic photon entangler using a charged quantum dot inside a microcavity. *Physical Review B*, 78(12):125318, 2008.

[95] CY Hu, WJ Munro, JL OBrien, and JG Rarity. Proposed entanglement beam splitter using a quantum-dot spin in a double-sided optical microcavity. *Physical Review B*, 80(20):205326, 2009.

[96] AB Young, CY Hu, and JG Rarity. Generating entanglement with low-q-factor microcavities. *Physical Review A*, 87(1):012332, 2013.

[97] Masayuki Shirane, Shunsuke Kono, Jun Ushida, Shunsuke Ohkouchi, Naoki Ikeda, Yoshimasa Sugimoto, and Akihisa Tomita. Mode identification of high-quality-factor single-defect nanocavities in quantum dot-embedded photonic crystals. *arXiv preprint cond-mat/0702234*, 2007.

[98] K Hennessy, C Högerle, E Hu, A Badolato, and A Imamoğlu. Tuning photonic nanocavities by atomic force microscope nano-oxidation. *Applied physics letters*, 89(4):041118, 2006.

[99] IJ Luxmoore, ED Ahmadi, AM Fox, M Hugues, and MS Skolnick. Unpolarized h1 photonic crystal nanocavities fabricated by stretched lattice design. *Applied Physics Letters*, 98(4):041101, 2011.

[100] IJ Luxmoore, ED Ahmadi, BJ Luxmoore, NA Wasley, AI Tartakovskii, M Hugues, MS Skolnick, and AM Fox. Restoring mode degeneracy in h1 photonic crystal cavities by uniaxial strain tuning. *Applied Physics Letters*, 100(12):121116, 2012.

[101] Timothy M Sweeney, Samuel G Carter, Allan S Bracker, Mijin Kim, Chul Soo Kim, Lily Yang, Patrick M Vora, Peter G Brereton, Erin R Cleveland, and Daniel Gammon. Cavity-stimulated raman emission from a single quantum dot spin. *Nature Photonics*, 8(6):442–447, 2014.

[102] Kazuki Koshino, Satoshi Ishizaka, and Yasunobu Nakamura. Deterministic photon-photon swap gate using a λ system. *Physical Review A*, 82(1):010301, 2010.

[103] Michael A Nielsen and Isaac L Chuang. *Quantum computation and quantum information*. Cambridge university press, 2010.

[104] Lov K Grover. A fast quantum mechanical algorithm for database search. In *Proceedings of the twenty-eighth annual ACM symposium on Theory of computing*, pages 212–219. ACM, 1996.

[105] Daniel R Simon. On the power of quantum computation. *SIAM journal on computing*, 26(5):1474–1483, 1997.

[106] Peter W Shor. Polynomial-time algorithms for prime factorization and discrete logarithms on a quantum computer. *SIAM review*, 41(2):303–332, 1999.

[107] Valerio Scarani, Helle Bechmann-Pasquinucci, Nicolas J Cerf, Miloslav Dušek, Norbert Lütkenhaus, and Momtchil Peev. The security of practical quantum key distribution. *Reviews of modern physics*, 81(3):1301, 2009.

[108] Daniel A Lidar and Todd A Brun. *Quantum error correction*. Cambridge University Press, 2013.

[109] Charles H Bennett, Gilles Brassard, Claude Crépeau, Richard Jozsa, Asher Peres, and William K Wootters. Teleporting an unknown quantum state via dual classical and einstein-podolsky-rosen channels. *Physical review letters*, 70(13):1895, 1993.

[110] Bas Hensen, H Bernien, AE Dréau, A Reiserer, N Kalb, MS Blok, J Ruitenberg, RFL Vermeulen, RN Schouten, C Abellán, et al. Loophole-free bell inequality violation using electron spins separated by 1.3 kilometres. *Nature*, 526(7575):682–686, 2015.

[111] A Fuhrmanek, R Bourgain, Yvan RP Sortais, and A Browaeys. Free-space lossless state detection of a single trapped atom. *Physical review letters*, 106(13):133003, 2011.

[112] AH Myerson, DJ Szwer, SC Webster, DTC Allcock, MJ Curtis, G Imreh, JA Sherman, DN Stacey, AM Steane, and DM Lucas. High-fidelity readout of trapped-ion qubits. *Physical Review Letters*, 100(20):200502, 2008.

[113] TP Harty, DTC Allcock, CJ Ballance, L Guidoni, HA Janacek, NM Linke, DN Stacey, and DM Lucas. High-fidelity preparation, gates, memory, and readout of a trapped-ion quantum bit. *Physical review letters*, 113(22):220501, 2014.

[114] Philipp Neumann, Johannes Beck, Matthias Steiner, Florian Rempp, Helmut Fedder, Philip R Hemmer, Jörg Wrachtrup, and Fedor Jelezko. Single-shot readout of a single nuclear spin. *Science*, 329(5991):542–544, 2010.

[115] Lucio Robledo, Lilian Childress, Hannes Bernien, Bas Hensen, Paul FA Alkemade, and Ronald Hanson. High-fidelity projective read-out of a solid-state spin quantum register. *Nature*, 477(7366):574–578, 2011.

[116] AN Vamivakas, C-Y Lu, C Matthiesen, Y Zhao, S Fält, A Badolato, and M Atatüre. Observation of spin-dependent quantum jumps via quantum dot resonance fluorescence. *Nature*, 467(7313):297–300, 2010.

[117] YM Kim, D Sleiter, K Sanaka, Y Yamamoto, J Meijer, K Lischka, and A Pawlis. Semiconductor qubits based on fluorine implanted znmgse/znse quantum-well nanostructures. *Physical Review B*, 85(8):085302, 2012.

[118] Lachlan J Rogers, Kay D Jahnke, Marcus W Doherty, Andreas Dietrich, Liam P McGuinness, Christoph Müller, Tokuyuki Teraji, Hitoshi Sumiya, Junichi Isoya, Neil B Manson, et al. Electronic structure of the negatively charged silicon-vacancy center in diamond. *Physical Review B*, 89(23):235101, 2014.

[119] Lachlan J Rogers, Kay D Jahnke, Mathias H Metsch, Alp Sipahigil, Jan M Binder, Tokuyuki Teraji, Hitoshi Sumiya, Junichi Isoya, Mikhail D Lukin, Philip Hemmer, et al. All-optical initialization, readout, and coherent preparation of single silicon-vacancy spins in diamond. *Physical review letters*, 113(26):263602, 2014.

[120] Joerg Bochmann, Martin Mücke, Christoph Guhl, Stephan Ritter, Gerhard Rempe, and David L Moehring. Lossless state detection of single neutral atoms. *Physical review letters*, 104(20):203601, 2010.

[121] Roger Gehr, Jürgen Volz, Guilhem Dubois, Tilo Steinmetz, Yves Colombe, Benjamin L Lev, Romain Long, Jérôme Estève, and Jakob Reichel. Cavity-based single atom preparation and high-fidelity hyperfine state readout. *Physical review letters*, 104(20):203602, 2010.

[122] A Young, CY Hu, L Marseglia, JP Harrison, JL O'Brien, and JG Rarity. Cavity enhanced spin measurement of the ground state spin of an nv center in diamond. *New Journal of Physics*, 11(1):013007, 2009.

[123] Mitsuro Sugita, Susumu Machida, and Yoshihisa Yamamoto. Quantum nondemolition measurement of a single electron spin in a quantum dot. *arXiv preprint quant-ph/0301064*, 2003.

[124] Shruti Puri, Peter L McMahon, and Yoshihisa Yamamoto. Single-shot quantum nondemolition measurement of a quantum-dot electron spin using cavity exciton-polaritons. *Physical Review B*, 90(15):155421, 2014.

[125] Yasuhiko Arakawa, Satoshi Iwamoto, Masahiro Nomura, Aniwat Tandaechanurat, and Yasutomo Ota. Cavity quantum electrodynamics and lasing oscillation in single quantum dot-photonic crystal nanocavity coupled systems. *IEEE Journal of Selected Topics in Quantum Electronics*, 18(6):1818–1829, 2012.

[126] Sylvain Combrié, Alfredo De Rossi, et al. Directive emission from high-q photonic crystal cavities through band folding. *Physical Review B*, 79(4):041101, 2009.

[127] Simone L Portalupi, Matteo Galli, Christopher Reardon, TF Krauss, Liam OFaolain, Lucio C Andreani, and Dario Gerace. Planar photonic crystal cavities with far-field optimization for high coupling efficiency and quality factor. *Optics express*, 18(15):16064–16073, 2010.

[128] Hiroyuki Takagi, Yasutomo Ota, Naoto Kumagai, Satomi Ishida, Satoshi Iwamoto, and Yasuhiko Arakawa. High q h1 photonic crystal nanocavities with efficient vertical emission. *Optics express*, 20(27):28292–28300, 2012.

[129] TG Tiecke, KP Nayak, JD Thompson, T Peyronel, NP De Leon, V Vuletić, and MD Lukin. Efficient fiber-optical interface for nanophotonic devices. *Optica*, 2(2):70–75, 2015.

[130] O Gazzano, S Michaelis de Vasconcellos, C Arnold, A Nowak, E Galopin, I Sagnes, L Lanco, A Lemaître, and P Senellart. Bright solid-state sources of indistinguishable single photons. *Nature communications*, 4:1425, 2013.

[131] N Somaschi, V Giesz, L De Santis, JC Loredo, MP Almeida, G Hornecker, SL Portalupi, T Grange, C Anton, J Demory, et al. Near-optimal single-photon sources in the solid state. *Nature Photonics*, 2016.

[132] Robert H Hadfield. Single-photon detectors for optical quantum information applications. *Nature photonics*, 3(12):696–705, 2009.

[133] Yasutomo Ota, Masayuki Shirane, Masahiro Nomura, Naoto Kumagai, Satomi Ishida, Satoshi Iwamoto, Shinichi Yorozu, and Yasuhiko Arakawa. Vacuum rabi splitting with a single quantum dot embedded in a h1 photonic crystal nanocavity. *Applied Physics Letters*, 94(3):3102, 2009.

[134] Ryuichi Ohta, Yasutomo Ota, Masahiro Nomura, Naoto Kumagai, Satomi Ishida, Satoshi Iwamoto, and Yasuhiko Arakawa. Strong coupling between a photonic crystal nanobeam cavity and a single quantum dot. *Applied Physics Letters*, 98(17):3104, 2011.

[135] Evelin Weidner, Sylvain Combrié, Alfredo De Rossi, Julien Nagle, Simone Cassette, Anne Talneau, Henri Benisty, et al. Achievement of ultrahigh quality factors in gaas photonic crystal membrane nanocavity. *Applied physics letters*, 89(22):221104, 2006.

[136] Sylvain Combrié, Alfredo De Rossi, Quynh Vy Tran, and Henri Benisty. Gaas photonic crystal cavity with ultrahigh q: microwatt nonlinearity at 1.55 μm. *Optics letters*, 33(16):1908–1910, 2008.

[137] Daniel Loss and David P DiVincenzo. Quantum computation with quantum dots. *Physical Review A*, 57(1):120, 1998.

[138] Christoph Kloeffel and Daniel Loss. Prospects for spin-based quantum computing in quantum dots. *Annual Review of Condensed Matter Physics*, 4:51–81, 2013.

[139] A Laucht, F Hofbauer, N Hauke, J Angele, Søren Stobbe, M Kaniber, G Böhm, Peter Lodahl, MC Amann, and JJ Finley. Electrical control of spontaneous emission and strong coupling for a single quantum dot. *New Journal of Physics*, 11(2):023034, 2009.

[140] S Reitzenstein, S Münch, P Franeck, A Rahimi-Iman, A Löffler, S Höfling, L Worschech, and A Forchel. Control of the strong light-matter interaction between an elongated in 0.3 ga 0.7 as quantum dot and a micropillar cavity using external magnetic fields. *Physical review letters*, 103(12):127401, 2009.

[141] Hyochul Kim, Deepak Sridharan, Thomas C Shen, Glenn S Solomon, and Edo Waks. Strong coupling between two quantum dots and a photonic crystal cavity using magnetic field tuning. *Optics express*, 19(3):2589–2598, 2011.

[142] Hyochul Kim, Thomas C Shen, Deepak Sridharan, Glenn S Solomon, and Edo Waks. Magnetic field tuning of a quantum dot strongly coupled to a photonic crystal cavity. *Applied Physics Letters*, 98(9):091102, 2011.

[143] Paola Borri, Wolfgang Langbein, Stephan Schneider, Ulrike Woggon, Roman L Sellin, Dongxun Ouyang, and Dieter Bimberg. Ultralong dephasing time in ingaas quantum dots. *Physical Review Letters*, 87(15):157401, 2001.

[144] J Förstner, C Weber, J Danckwerts, and A Knorr. Phonon-assisted damping of rabi oscillations in semiconductor quantum dots. *Physical review letters*, 91(12):127401, 2003.

[145] AJ Ramsay, Achanta Venu Gopal, EM Gauger, A Nazir, Brendon William Lovett, AM Fox, and MS Skolnick. Damping of exciton rabi rotations by acoustic phonons in optically excited ingaas/gaas quantum dots. *Physical review letters*, 104(1):017402, 2010.

[146] SM Ulrich, S Ates, S Reitzenstein, A Löffler, A Forchel, and P Michler. Dephasing of triplet-sideband optical emission of a resonantly driven inas/gaas quantum dot inside a microcavity. *Physical review letters*, 106(24):247402, 2011.

[147] C Roy and S Hughes. Phonon-dressed mollow triplet in the regime of cavity quantum electrodynamics: excitation-induced dephasing and nonperturbative cavity feeding effects. *Physical review letters*, 106(24):247403, 2011.

[148] JJ Finley, M Sabathil, P Vogl, G Abstreiter, R Oulton, AI Tartakovskii, DJ Mowbray, MS Skolnick, SL Liew, AG Cullis, et al. Quantum-confined stark shifts of charged exciton complexes in quantum dots. *Physical Review B*, 70(20):201308, 2004.

[149] Stefan Seidl, Martin Kroner, Alexander Högele, Khaled Karrai, Richard J Warburton, Antonio Badolato, and Pierre M Petroff. Effect of uniaxial stress on excitons in a self-assembled quantum dot. *Applied Physics Letters*, 88(20):203113, 2006.

[150] Tim Zander, Andreas Herklotz, Suwit Kiravittaya, Mohamed Benyoucef, Fei Ding, Paola Atkinson, Santosh Kumar, Johannes D Plumhof, Kathrin Dörr, Armando Rastelli, et al. Epitaxial quantum dots in stretchable optical microcavities. *Optics express*, 17(25):22452–22461, 2009.

[151] F Ding, R Singh, JD Plumhof, T Zander, V Křápek, YH Chen, M Benyoucef, V Zwiller, K Dörr, G Bester, et al. Tuning the exciton binding energies in single self-assembled ingaas/gaas quantum dots by piezoelectric-induced biaxial stress. *Physical review letters*, 104(6):067405, 2010.

[152] Ranber Singh and Gabriel Bester. Lower bound for the excitonic fine structure splitting in self-assembled quantum dots. *Physical review letters*, 104(19):196803, 2010.

[153] Garnett W Bryant, M Zieliński, Natalia Malkova, James Sims, W Jaskólski, and Javier Aizpurua. Effect of mechanical strain on the optical properties of quantum dots: controlling exciton shape, orientation, and phase with a mechanical strain. *Physical review letters*, 105(6):067404, 2010.

[154] Johannes David Plumhof, Vlastimil Křápek, Fei Ding, KD Jöns, R Hafenbrak, Petr Klenovskỳ, A Herklotz, K Dörr, P Michler, Armando Rastelli, et al. Strain-induced anticrossing of bright exciton levels in single self-assembled gaas/al x ga 1- x as and in x ga 1- x as/gaas quantum dots. *Physical Review B*, 83(12):121302, 2011.

[155] Ming Gong, Weiwei Zhang, Guang-Can Guo, and Lixin He. Exciton polarization, fine-structure splitting, and the asymmetry of quantum dots under uniaxial stress. *Physical review letters*, 106(22):227401, 2011.

[156] Cristian Bonato, Evert van Nieuwenburg, Jan Gudat, Susanna Thon, Hyochul Kim, Martin P van Exter, and Dirk Bouwmeester. Strain tuning of quantum dot optical transitions via laser-induced surface defects. *Physical Review B*, 84(7):075306, 2011.

[157] S Kumar, R Trotta, E Zallo, JD Plumhof, P Atkinson, A Rastelli, and OG Schmidt. Strain-induced tuning of the emission wavelength of high quality gaas/algaas quantum dots in the spectral range of the 87rb d2 lines. *Applied Physics Letters*, 99(16):161118, 2011.

[158] Hsuan Lin, Chia-Hsien Lin, Wei-Chen Lai, Yi-Shan Lee, Sheng-Di Lin, and Wen-Hao Chang. Stress tuning of strong and weak couplings between quantum dots and cavity modes in microdisk microcavities. *Physical Review B*, 84(20):201301, 2011.

[159] K. D. Jöns, R. Hafenbrak, R. Singh, F. Ding, J. D. Plumhof, A. Rastelli, O. G. Schmidt, G. Bester, and P. Michler. Dependence of the redshifted and blueshifted photoluminescence spectra of single $in_xga_{1-x}As$/GaAs quantum dots on the applied uniaxial stress. *Phys. Rev. Lett.*, 107:217402, Nov 2011.

[160] R Trotta, Paola Atkinson, JD Plumhof, E Zallo, Roman Olegovich Rezaev, S Kumar, S Baunack, JR Schröter, A Rastelli, and OG Schmidt. Nanomembrane quantum-light-emitting diodes integrated onto piezoelectric actuators. *Advanced materials*, 24(20):2668–2672, 2012.

[161] Bui Thanh Tung, Dzung Viet Dao, Taro Ikeda, Yoshiaki Kanamori, Kazuhiro Hane, and Susumu Sugiyama. Investigation of strain sensing effect in modified single-defect photonic crystal nanocavity. *Optics express*, 19(9):8821–8829, 2011.

[162] Christopher E Kuklewicz, Ralph NE Malein, Pierre M Petroff, and Brian D Gerardot. Electro-elastic tuning of single particles in individual self-assembled quantum dots. *Nano letters*, 12(7):3761–3765, 2012.

[163] C Schneider, M Strauß, T Sünner, A Huggenberger, D Wiener, S Reitzenstein, M Kamp, S Höfling, and A Forchel. Lithographic alignment to site-controlled quantum dots for device integration. *Applied Physics Letters*, 92(18):183101, 2008.

[164] Michael K Yakes, Lily Yang, Allan S Bracker, Timothy M Sweeney, Peter G Brereton, Mijin Kim, Chul Soo Kim, Patrick M Vora, Doewon Park, Samuel G Carter, et al. Leveraging crystal anisotropy for deterministic growth of inas quantum dots with narrow optical linewidths. *Nano letters*, 13(10):4870–4875, 2013.

[165] Sonia Buckley, Kelley Rivoire, and Jelena Vučković. Engineered quantum dot single-photon sources. *Reports on Progress in Physics*, 75(12):126503, 2012.

[166] F Jelezko and J Wrachtrup. Single defect centres in diamond: A review. *physica status solidi (a)*, 203(13):3207–3225, 2006.

[167] David D Awschalom, Lee C Bassett, Andrew S Dzurak, Evelyn L Hu, and Jason R Petta. Quantum spintronics: engineering and manipulating atom-like spins in semiconductors. *Science*, 339(6124):1174–1179, 2013.

[168] CW Thiel, Thomas Böttger, and RL Cone. Rare-earth-doped materials for applications in quantum information storage and signal processing. *Journal of luminescence*, 131(3):353–361, 2011.

[169] Ajit Srivastava, Meinrad Sidler, Adrien V Allain, Dominik S Lembke, Andras Kis, and A Imamoğlu. Optically active quantum dots in monolayer wse2. *Nature nanotechnology*, 10(6):491–496, 2015.

[170] Yu-Ming He, Genevieve Clark, John R Schaibley, Yu He, Ming-Cheng Chen, Yu-Jia Wei, Xing Ding, Qiang Zhang, Wang Yao, Xiaodong Xu, et al. Single quantum emitters in monolayer semiconductors. *Nature nanotechnology*, 10(6):497–502, 2015.

[171] M Koperski, K Nogajewski, A Arora, V Cherkez, P Mallet, J-Y Veuillen, J Marcus, P Kossacki, and M Potemski. Single photon emitters in exfoliated wse2 structures. *Nature nanotechnology*, 10(6):503–506, 2015.

[172] Chitraleema Chakraborty, Laura Kinnischtzke, Kenneth M Goodfellow, Ryan Beams, and A Nick Vamivakas. Voltage-controlled quantum light from an atomically thin semiconductor. *Nature nanotechnology*, 10(6):507–511, 2015.